Journal of Geophysical Research: Oceans

RESEARCH ARTICLE
10.1002/2017JC013582

Modulation of the Semidiurnal Cycle of Turbulent Dissipation by Wind-Driven Upwelling in a Coastal Embayment

Bieito Fernández-Castro[1], Miguel Gilcoto[2], Alberto C. Naveira-Garabato[3], Marina Villamaña[4], Rocío Graña[2], and Beatriz Mouriño-Carballido[4]

[1]Laboratorio de Xeoquímica Orgánica. Instituto de Investigacións Mariñas (IIM-CSIC), Rúa Eduardo Cabello, 6, Vigo, Spain, [2]Grupo de Oceanoloxía. Instituto de Investigacións Mariñas (IIM-CSIC), Rúa Eduardo Cabello, 6, Vigo, Spain, [3]Ocean and Earth Science, University of Southampton, National Oceanography Centre, Southampton, U.K, [4]Departamento de Ecoloxía e Bioloxía Animal, Universidade de Vigo, Vigo, Spain

Key Points:
- The semidiurnal cycle of turbulent dissipation in a partially-mixed coastal embayment results from upwelling-tide interaction
- The overall intensity of turbulent dissipation is modulated by the rate of coastal upwelling
- This mechanism acts as a pathway for nutrient supply from deep upwelled to sunlit surface waters

Correspondence to:
B. Fernández Castro,
bieitof@iim.csic.es;
bieito.fernandez@uvigo.es

Citation:
Fernández-Castro, B., Gilcoto, M., Naveira-Garabato, A. C., Villamaña, M., Graña, R., & Mouriño-Carballido, B. (2018). Modulation of the semidiurnal cycle of turbulent dissipation by wind-driven upwelling in a coastal embayment. *Journal of Geophysical Research: Oceans*, *123*, 4034–4054. https://doi.org/10.1002/2017JC013582

Received 13 DEC 2017
Accepted 28 APR 2018
Accepted article online 6 MAY 2018
Published online 18 JUN 2018

Abstract With two 25-hour series of turbulent microstructure and currents observations carried out in August 2013, during spring (CHAOS 1) and neap tides (CHAOS 2), we investigated the semidiurnal cycle of turbulent dissipation in an embayment affected by coastal upwelling (Ría de Vigo, NW Iberia). At the time of sampling, the bay hosted a net, wind-driven bi-directional positive exchange flow and thermal stratification. Turbulent kinetic energy (TKE) dissipation (ε) at the interface between upwelled and surface waters was enhanced by two orders of magnitude during the ebbs ($\sim 10^{-6}$ W kg^{-1}) with respect to the floods ($\sim 10^{-8}$ W kg^{-1}). This pattern was caused by the constructive interference of the shear associated with the upwelling and tidal currents. The vertical structure of the tidal currents was consistent with a deformation of tidal ellipses by stratification, which was tightly coupled to the intensity of upwelling. This two-pronged interaction resulted in a modulation of the semidiurnal cycle of turbulent dissipation by coastal upwelling. Thus, as a result of the upwelling relaxation conditions experienced during CHAOS 1, depth-integrated interior TKE dissipation rates were higher, by a factor of $\sim$2, compared to CHAOS 2. By using a simple model, we determined that observed variations in turbulent mixing had a limited influence on the tidal variations of stratification, which were dominated by straining and advection. The mixing mechanism described here is potentially relevant for the ecology of upwelling bays, as it can stimulate the transport of nutrients from deep-upwelled waters to the sun-lit surface layers where primary production takes place.

1. Introduction

Turbulent mixing is the dominant mechanism involved in the transfer of heat, momentum and dissolved substances in the ocean. The intensity of turbulent dissipation depends on a trade-off between production by shear and suppression by stratification. Conversely, turbulence influences the stability of the water column through an ongoing competition with buoyancy inputs (Thorpe, 2007). Despite representing only $\sim$8% of the ocean, about 75% of the ocean's energy dissipation takes place in the coastal regions (Munk & Wunsch, 1998). These environments, particularly estuaries and bays, are highly dynamic as stratification and mixing conditions can radically vary within a few hours, e.g. over a tidal cycle (Simpson et al., 1990). This variability has important implications for the functioning of physical (e.g. Burchard & Hetland, 2010; Jay & Musiak, 1996; Scully & Friedrichs, 2007) and ecological processes (e.g., Barton et al., 2016; Villamaña et al., 2017) operating in these systems.

In the classical momentum and stratification balances for estuaries, turbulence generated by tidal bottom friction was considered the main term counteracting the effects of the acceleration by the horizontal density gradient and straining of the density field (Hansen & Rattray, 1966; Simpson et al., 1990). However, decades of research have demonstrated that turbulence generated away from the bottom boundary -internal mixing- can also play a major role in many estuaries (e.g., Kay & Jay, 2003a; Peters, 1997; Peters & Bokhorst, 2000). The dynamics of interior turbulent mixing are linked to the two-way interactions between shear and stratification (Jay & Musiak, 1996; Peters, 1997; Rippeth et al., 2001). In the presence of a horizontal density gradient, straining by sheared currents can either increase or decrease stratification depending on the relative orientation of the shear and density gradient vectors (Simpson et al., 1990). In estuaries, differential advection by positive estuarine circulation and sheared ebb tidal currents tends to increase stratification, whereas sheared flood currents tend to suppress it. As a result, an intratidal asymmetry in the stratification

conditions is created with reduced stratification during the floods, potentially resulting in gravitational instabilities and enhanced dissipation (Rippeth et al., 2001).

Besides that, shear-instability mixing can occur when shear is strong enough to overcome the existing stratification (Geyer & Smith, 1987; Rippeth et al., 2005). In this case, atypical cycles of internal turbulent mixing can be observed where strong turbulence, frequently during the ebbs, is not coincident with reduced stratification (Whitney et al., 2012). This situation is typical of permanently stratified and salt wedge estuaries where a strong density interface supports shear instabilities (Geyer & Smith, 1987; Kay & Jay, 2003b; Partch & Smith, 1978). Ebb-enhanced shear-driven dissipation has been attributed to variations in the tidal shear due to the positive interference with the barotropic and gravitational subtidal circulation (Jay & Musiak, 1996; Kay & Jay, 2003b). Furthermore, other components of the flow such as wind-driven circulation (Rippeth et al., 2009; Scully et al., 2005) or internal waves (McCardell et al., 2016) can increase shear and mixing. As a result of this complexity, the turbulence dynamics strongly differ from one system to another, and in space and time within the same system, depending on the nature, timing and relative strength of the sources of stratification and shear (Whitney et al., 2012).

The Ría de Vigo is the southernmost of the Rías Baixas, four semi-enclosed elongated bays found in Galicia, NW Iberia, in the Northern limit of the Iberian-Canary current Eastern Boundary Upwelling Ecosystem (EBUE) (Fréon et al., 2009; Wooster et al., 1976). The Ría de Vigo has been historically classified as a partially mixed estuary (Fraga & Margalef, 1979; Prego & Fraga, 1990), although it shows some particular features. The most outstanding characteristic is that the subtidal circulation is controlled, in most situations, by wind-driven coastal upwelling-downwelling events over the adjacent continental shelf. The Ría responds to these events through a bi-directional exchange flow along its main channel (Barton et al., 2015; Gilcoto et al., 2001; Piedracoba, 2005; Souto et al., 2003), a response that is reinforced and accelerated by local winds (Gilcoto et al., 2017). Under Equatorward upwelling-favorable winds, predominant from April to September, the Ría exhibits positive circulation, as the cool ($T \lesssim 13\,^{\circ}C$), salty ($S \sim 35.7-35.8$), nutrient-rich Eastern North Atlantic Central Water (ENACW) intrudes as a lower layer into the Ría, and the inner surface waters flush toward the ocean (Álvarez-Salgado et al., 1993; Fraga, 1981). As a result of this circulation pattern and enhanced solar radiation, the Ría is thermally stratified during the summer season (e.g., Nogueira et al., 1997). The rise of nutrient-rich waters into the sheltered Rías stimulates the growth of phytoplankton, which supports a highly productive food chain and one of the most economically important marine industries in Europe (Blanton et al., 1987; Figueiras et al., 2002). The bi-directional circulation reverses under southerly downwelling-favorable winds (Barton et al., 2016; Wooster et al., 1976), prevailing from October to March, as warm and salty surface waters of subtropical origin pile on the shelf (Haynes & Barton, 1990).

Previous studies of partially mixed estuaries have frequently described cycles of turbulence dominated by tidal bottom friction (Stacey & Ralston, 2005; Stacey et al., 1999), but also by interior processes, such as tidal and wind-driven straining (Chen & Sanford, 2009; Scully et al., 2005; Simpson et al., 2005; Xie & Li, 2018) and interfacial shear instabilities of the tidal flow (Peters, 1997; Peters & Bokhorst, 2000). Other studies have demonstrated that the interaction of the wind-driven upwelling circulation with other shear sources (i.e. internal waves) results in periods of relatively enhanced mixing in open coastal upwelling systems (e.g., the Oregon Shelf) (Avicola et al., 2007; Kurapov et al., 2010). Despite this evidence, the temporal variability of turbulent dissipation in estuaries and bays affected by wind-driven coastal upwelling is currently unknown. Here, we analyze a set of observations of turbulent microstructure and currents, carried out in the Ría de Vigo during spring and neap tides in August 2013, to evaluate the role of coastal upwelling in shaping the tidal cycle of turbulent dissipation. We demonstrate that significant dissipation occurs away from the bottom boundary during the ebbs, and that it results from the interplay between the tidal and the bi-directional upwelling shears.

2. Methods

2.1. Sampling Site

The Ría de Vigo, located at 42.2 °N, is about 33 km long, 15 km wide at the mouth and 40 m deep in the central channel. Northern (2.5 km wide by 23 m deep) and southern (5 km wide and 52 m deep) channels separated by the Cíes Islands afford communication between the Ría de Vigo and the shelf (Figure 1). In the framework of the CHAOS (Control of tHe structure of marine phytoplAnkton cOmmunities by turbulence and nutrient supply dynamicS) project two cruises were conducted on board the R/V *Mytilus* in the southern

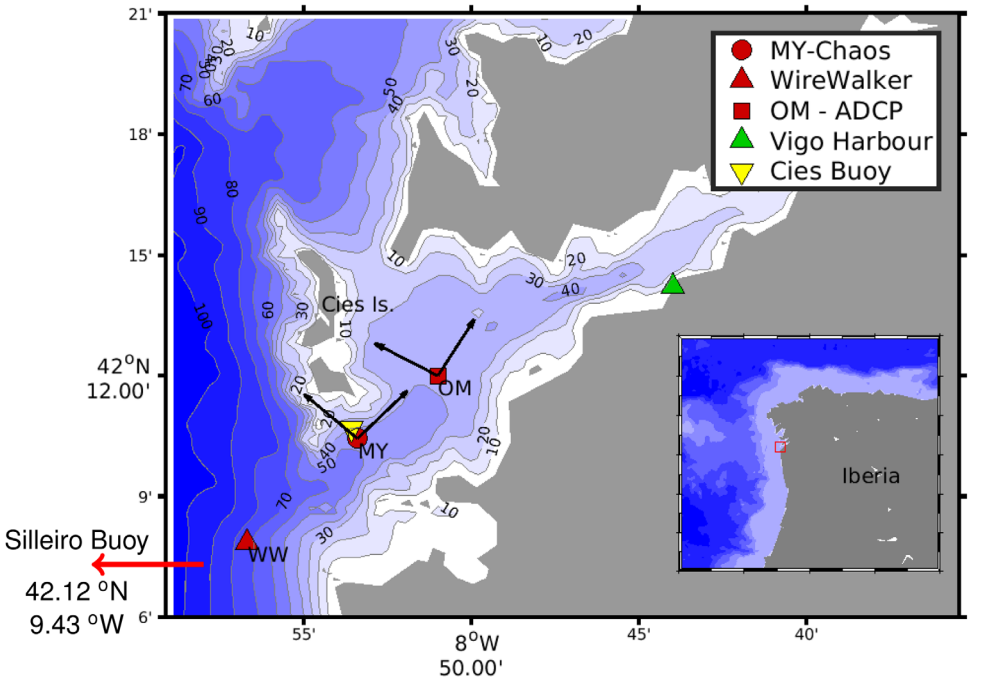

Figure 1. Map of the Ría de Vigo showing the location of the sampling sites. The red square, triangle, circle symbols represent the location of the upward-looking moored ADCP (OM, 42.20 °N-8.85 °W), the WireWalker mooring (WW, 42.13 °N-8.95 °W) and the intensive observations (CHAOS 1 - spring tides, CHAOS 2 - neap tides) carried out on board of the R/V *Mytilus* (MY, 42.17 °N-8.89 °W), respectively. The position of the Vigo Harbour and the Cíes meteorological buoy (used as a reference for local winds) are also indicated. Black arrows indicate the directions along and across the main axis of the Ría at the MY (45° North of East) and OM (65° North of East) sites, the red arrow indicates the position of the Silleiro Buoy (outside the map limits) and inset numbers indicate the depths of the isobaths.

mouth of the Ría de Vigo (42.17 °N-8.89 °W, MY site) in August 2013, during the summer upwelling season. During both cruises hydrography, turbulence microsctructure and currents measurements were recorded continuously over one complete diurnal tidal cycle (25 h). The first cruise (CHAOS 1, 20–21 August 2013) was conducted during spring tides, with a tidal amplitude of 3.3 m, and the second cruise (CHAOS 2, 27–28 August 2013) was conducted during neap tides, with a tidal amplitude of 1.7 m. The water depth at the sampling location was ∼45 m [see Villamaña et al., 2017, for details].

2.2. Microstructure Data Acquisition

Hydrographic (temperature and salinity) and microstructure shear and temperature data were obtained with an intensive yo-yo sampling using a turbulence microstructure profiler (MSS, (Prandke & Stips, 1998)). A total number of 402 microstructure profiles were collected during each cruise with a mean lag between profiles of 3.75 min. The microstructure sampling was interrupted every hour for vessel repositioning and to cast a CTD/rosette for water collection. The MSS profiler was equipped with two microsctructure shear sensors (type PNS06), a microstructure temperature sensor (FP07), a high-precision CTD probe and also a sensor to measure the horizontal acceleration of the profiler. The frequency of data sampling was 1024 Hz. The profiler was carefully balanced to have negative buoyancy in the water column and a sinking velocity of $\sim 0.4-0.7$ m s^{-1}. The shear sensors were calibrated before the cruise and the sensitivity was checked after each cast during the data processing.

Turbulent kinetic energy (TKE) dissipation rates (ε) were computed in 512 data point segments, with 50% overlap, from the shear variance under the assumption of isotropic turbulence using the following equation:

$$\varepsilon = 7.5\nu \left\langle \left(\frac{\partial u}{\partial z}\right)^2 \right\rangle, (\mathrm{W\,Kg^{-1}}) \quad (1)$$

where ν is the kinematic viscosity of seawater, $\partial u/\partial z$ the vertical shear and $\langle\,.\,\rangle$ represents the ensemble average. The shear variance was computed by integrating the shear power spectrum. The lower integration

limit was determined by considering the size of the bins, and set to 2 cpm. The upper cut-off wavenumber for the integration of the shear spectrum was set as the Kolmogoroff number ($k_c = 1/(2\pi) \cdot (\varepsilon/\nu^3)^{1/4}$, cpm). An iterative procedure was applied to determine k_c. The maximum upper cut-off was not allowed to exceed 30 cpm to avoid the noisy part of the spectrum. Assuming a universal form of the shear spectrum (Nasmyth), ε was corrected for the loss of variance below and above the used integration limits, using the polynomial functions reported by Prandke et al. (). Dissipation spikes were removed by comparing the dissipation rates computed simultaneously from the two shear sensors. When the value of ε computed with one sensor exceeded by a factor of two the value computed with the other sensor, the former was discarded. The data was visually checked afterward and the potentially contaminated data segments were removed.

In addition, Thorpe length-scales (L_T) (Thorpe, 1977) were calculated as the root-mean-square of the Thorpe displacements, computed after resorting the microstructure temperature profile obtained with the FP07 sensor of the MSS profiler. All the data provided by the MSS profiler were averaged in 1 m bins during data processing. During this averaging outliers (values exceeding the standard deviation by a factor of 2.7) were removed. Due to significant turbulence generation close to the ship, the microstructure shear and temperature data were considered reliable only below 7 m from the sea surface.

2.3. Current and Ancillary Data Acquisition

Current velocity data at the MY site were recorded during the field cruises using the vessel mounted RD Instruments 300 KHz Acoustic Doppler Profiler (vmADCP) on board the R/V *Mytilus*. The vmADCP was set up to average velocity measurements (pings) every two minutes (43 pings/ensemble). These measurements were made in layers with a bin thickness of 1 m and with the first bin located at 4.5 m below sea surface. Absolute velocities were calculated by referencing the measured velocities to the bottom track. Data processing was carried out with the WinADCP software. Velocity data was checked and bad-quality data (Percent good $<$95%) and spikes were removed. Zonal and meridional velocity vector components were projected onto two axis along (u) and across (v) the main channel of the Ría. The u and v components were positive to the Northeast (into the Ría) and to the Northwest, respectively (see Figure 1).

During the two cruises, a vertically profiling instrument package propelled by ocean waves, WireWalker (Rainville & Pinkel, 2001) equipped with a RBR CTD (model XR620), was deployed at the $\sim$70 m isobath outside the Ría, in front of the Southern mouth, 6.6 km to the South West of the MY site (42.13 °N-8.95 °W, WW site, Figure 1). This instrument performed 6Hz CTD measurements while continuously profiling the water column during 21 hours (198 and 278 full-depth profiles during CHAOS 1 and CHAOS 2, respectively).

Ancillary data include wind speed and direction record over the shelf, used as an indicator of upwelling and downwelling conditions, from the Silleiro Buoy (42.12 °N, 9.43 °W, data provided by Puertos del Estado, www.puertos.es), 45 km offshore. Long-term observations of current velocity from the STRAMIX research project were obtained with an upward-looking moored ADCP from Teledyne RD Instruments (WorkHorse 600 kHz ADCP). This instrument was bottom-moored in a gimballed anti-trawling pyramid for 72 days (20/06/2013 - 02/09/2013) at the main Ría channel 3.3 Km to the north-west of the MY site (42.20 °N-8.85 °W, OM site, Figure 1). Current measurements were made in 90 layers, at fixed distances from the ADCP ($\sim$ 0.6 mab, meters above bottom) of 0.5 m thickness each one, and ensemble averages of 85 pings were calculated every 10 minutes (Piñeiro Rodríguez, 2014). Subtidal residual currents were calculated by filtering out (super)tidal frequencies with a A24/25/25 filter (Godin, 1972).

2.4. Characterization of Turbulence

Data collected with the MSS (temperature, salinity, ε) and vmADCP (horizontal velocity) were bin-averaged to a common grid with a resolution of 2 m in the vertical dimension and 10 min in time. A 4-m and 60-min window was used for grid-averaging in the vertical and temporal dimensions, respectively. A mean value of 7 microstructure casts were averaged for each bin. During grid-averaging, outliers (values greater than the 95-percentile for each bin) were discarded. In this way smoothed fields of temperature, salinity, potential density, ε, u and v were produced. Using these data, additional variables were calculated to characterize the evolution of turbulence field along the tidal cycles, and to determine the mechanisms driving this variability.

The squared-buoyancy frequency, $N^2 = -g/\rho_0 \frac{\partial \rho}{\partial z}$, where g is the gravity acceleration and ρ is the seawater density derived from the CTD measurements carried out with the MSS profiler, was computed for each grid

bin by first-differences. The activity number or buoyancy Reynolds number (Ivey et al., 2008; Shih et al., 2005) ($Re_b = \varepsilon/\nu N^2$) was used investigate how turbulence behaved in relation to stratification (Gargett et al., 1984; Shih et al., 2005). This parameter can be interpreted as the ratio of the buoyancy time-scale ($1/N$) to the time it takes for turbulent events to fully develop ($\sqrt{\varepsilon/\nu}$) (Ivey et al., 2008). Bouffard and Boegman [2013] defined four turbulence regimes as a function of Re_b: molecular ($Re_b < 1.7$), buoyancy-controlled ($1.7 < Re_b < 8.5$), transitional ($8.5 < Re_b < 100$) and energetic ($Re_b > 100$). In the energetic regime turbulence is unaffected by stratification, while for the buoyancy-controlled and molecular regimes turbulence is suppressed by stratification. While the L_T provides an estimate of the "actual" size of the turbulent eddies, the Ozmidov length-scale ($L_O = \sqrt{\varepsilon/N^3}$) represents the scale for which buoyancy is in balance with inertia, i.e. the largest possible size for turbulent eddies without being affected by stratification. The ratio between both quantities defines the Froude turbulent number ($Fr_T = (L_O/L_T)^{2/3}$) (Ivey & Imberger, 1991). Large values of Fr_T correspond to weak influence of stratification, and for small numbers turbulence is likely decaying (Monismith, 2010).

In order to determine whether the observed stratified turbulence is driven by shear in the mean flow, the degree of shear instability was characterized using the gradient Richardson number, $\mathrm{Ri} = N^2/sh^2$, where sh^2 is squared vertical shear of the vmADCP-derived horizontal velocities, $sh^2 = \left(\frac{\partial u}{\partial z}\right)^2 + \left(\frac{\partial v}{\partial z}\right)^2$, computed for each grid bin by first-differences. Linear theory predicts that a flow may become unstable when Ri $<$0.25 (Miles, 1961). However, higher critical Ri values (0.25 $<$Ri $<$1) are possible too, particularly when the internal wave field interacts with the mean flow (e.g., Geyer & Smith, 1987).

2.5. Current Decomposition

In order to separate the influence of tidal and upwelling components in the vmADCP currents, the velocity vector was decomposed into a subtidal residual term, $\mathbf{u}^{\mathrm{R}}(z,t)$, related to the background upwelling circulation, and a tidal term of semidiurnal principal lunar frequency (M_2, 12.42 h), $\mathbf{u}^{M_2}(z,t)$. This was accomplished operationally by fitting the time-series of each velocity component to a harmonic function plus a "low-frequency" trend term:

$$\mathbf{u}(z,t) \sim \mathbf{A}(z)\cos\left(2\pi\omega_{M_2} + \boldsymbol{\delta}(z)\right) + \mathbf{B}(z)t + \mathbf{C}(z), \tag{2}$$

where $\mathbf{A}(z)$ is the amplitude, ω_{M_2} ($=2\pi/12.42\,\mathrm{h}^{-1}$) is the semidiurnal M_2 frequency, $\boldsymbol{\delta}$ is the phase, and $\mathbf{B}$ and $\mathbf{C}$ represent the coefficients of the linear and constant terms, respectively. We thus defined $\mathbf{u}^{M_2}(z,t) \equiv \mathbf{A}(z)\cos\left(2\pi\omega_{M_2} + \boldsymbol{\delta}\right)$, and $\mathbf{u}^{\mathrm{R}}(z,t) \equiv \mathbf{B}(z)t + \mathbf{C}(z)$. This fit represented on average 93% and 76% of the flow variance in the along-Ría axis during CHAOS 1 and CHAOS 2, respectively. The amplitudes and phases of the harmonic fit were used to calculate the tidal ellipse parameters (Maas & van Haren, 1987).

2.6. Energy Fluxes of Nonlinear Internal Waves

In order to estimate the potential contribution of non-linear internal waves (NIWs) to the observed turbulent dissipation during the CHAOS cruises, energy fluxes associated with these waves were calculated at the WW site (Figure 1). The computation was based on measurements carried out with a RBR CTD mounted on the WireWalker. The energy fluxes were calculated as:

$$\mathrm{F} = \mathrm{E}c_g \qquad (\mathrm{W\,m^{-1}}) \tag{3}$$

where E is the total energy content of the waves and c_g their group speed. E was calculated from potential energy assuming energy equipartition (E = PE + KE = 2 PE). The potential energy was calculated as:

$$\mathrm{PE}(z) = g^2\langle\rho'^2\rangle/2\rho_0\overline{N^2} \qquad (\mathrm{m^2\,s^{-2}}) \tag{4}$$

where $\rho' = \rho'(t,z)$ is the density perturbation ($\rho' = \rho - \overline{\rho}$, where $\overline{\rho} = \overline{\rho}(z)$ is a reference cruise-averaged density profile), $\overline{N^2} = \overline{N^2}(z)$ is the cruise-averaged buoyancy frequency profile, and $\langle\rho'^2\rangle$ represents the variance of the density perturbations. As we were interested in high frequency internal waves, $\langle\rho'^2\rangle$ was calculated by integrating the ρ' power spectrum over the high-frequency ($\nu > 1$ cph) range.

The non-linear phase (and group) speed of a weakly non-linear wave in a non rotating two layer fluid was calculated using the Korteweg-de-Vries (KdV) theory (Michallet & Barthelemy, 1998):

$$c = c_0\left(1 - \frac{\alpha\eta_0}{3c_0}\right) \tag{5}$$

In this equation, $\alpha = -\frac{3c_0}{2}\left(\frac{h_2 - h_1}{h_1 h_2}\right)$, where h_1 and h_2 are the upper and lower layer undisturbed thickness, η_0 is the maximum interface displacement, and c_0 is the phase speed of a linear internal wave:

$$c_0 = \sqrt{g' h_e} \tag{6}$$

where $g' = g\frac{\Delta\rho}{\rho_0}$ is the reduced gravity, where $\Delta\rho$ is the density difference between the upper an lower layers, and $h_e = \frac{h_1 h_2}{h}$, where $h = h_1 + h_2$ is the total water depth. The parameters used to perform the calculation, derived from the WireWalker measurements, were $h = 70$ m, $\rho_0 = 1027$ kg m^{-3}, $\Delta\rho = 0.5$ kg m^{-3}, $\eta_0 = 15$ m; and $h_1 = 5$ m (9 m), $h_2 = 65$ m (61 m) for CHAOS 1 (CHAOS 2).

2.7. The Stratification Balance

A simple model approach was used to calculate the horizontal density gradients and investigate the sources of the tidal variations of stratification during the CHAOS cruises. Tidal variations of the thermohaline vertical structure in estuaries have been successfully described as the result of the interplay between the straining of a non-uniform density field (Simpson et al., 1990), the advection of a non-uniform vertical stratification (Giddings et al., 2011; Scully & Geyer, 2012), and turbulent diffusion:

$$\frac{\partial N^2}{\partial t} = \underbrace{-\frac{\partial u}{\partial z}N_x^2 - \frac{\partial v}{\partial z}N_y^2 - \frac{\partial w}{\partial z}N^2}_{\text{straining}} \underbrace{-u\frac{\partial N^2}{\partial x} - v\frac{\partial N^2}{\partial y} - w\frac{\partial N^2}{\partial z}}_{\text{advection}} \underbrace{+\frac{\partial (K_\rho N^2)}{\partial z}}_{\text{diffusion}}, \tag{7}$$

where $N_x^2 = -\frac{g}{\rho_0}\frac{\partial \rho}{\partial x}$ is the horizontal buoyancy frequency, w is the vertical velocity and K_ρ is the diapycnal diffusivity. Determining the relative contribution of straining, advection and mixing to the buoyancy balance requires knowledge about the horizontal density gradients. Due to the lack of spatial resolution of the data collected during the CHAOS cruises, the horizontal density gradients were calculated from the local density variations using an inverse two-layer model approach. In order to minimize the effects of vertical advection and straining (the 3rd and 6th terms on the right-hand-side (rhs) of equarion (7), not considered in the model) the water column was divided into two layers separated by the 13.5 °C isotherm, representing the limit between deep-upwelled and surface waters. The density evolution in the upper (*U*) and lower (*L*) layers was modelled as:

$$\frac{\partial \rho^{U,L}}{\partial t} = -u^{U,L}\left(\frac{\partial \rho}{\partial x}\right)^{U,L} - v^{U,L}\left(\frac{\partial \rho}{\partial y}\right)^{U,L} \pm \left(-\frac{\rho}{g}\frac{\Gamma\langle\varepsilon\rangle}{h}\right) \tag{8}$$

where u and v are the averaged horizontal velocities, $\frac{\partial \rho}{\partial x}$ and $\frac{\partial \rho}{\partial y}$ are the horizontal density gradients, h was set to 20 m (about half of total water column depth) and $\langle\varepsilon\rangle$ is the TKE dissipation rate averaged in the interface between the upper and lower layers (13–14 °C). In the last term we used the Osborn [1980] equation ($K_\rho = \Gamma\varepsilon/N^2$, where $\Gamma \sim 0.25$ is the mixing efficiency (e.g. Kay & Jay, 2003b). The horizontal density gradients were calculated by least-square fitting to the observed variability of the averaged density in the upper and lower layers. Similarly to the approach followed to infer subtidal velocities, we allowed the density gradients to vary linearly with time, $\frac{\partial \rho}{\partial x} \sim \alpha + \beta \cdot t$. The evolution of N^2 was calculated by differentiating the equations of both layers, and the contribution of advection, straining and mixing were computed by rearranging the different terms.

3. Observations

3.1. Hydrographic Conditions

The synoptic wind and circulation conditions in the Ría de Vigo from a 12 day period including the two CHAOS cruises (13–30 August 2013) are shown in Figure 2. In general, shelf winds were northerly upwelling-favorable during most of the period. An initial upwelling event, with wind speed reaching 10 m s^{-1}, took place during 19 August followed by a relaxation and subsequent reversal between 20–22 August (Figure 2a). Afterwards, northerly winds re-intensified to a maximum of 15 m s^{-1} on 25 August and oscillated between 5 and 10 m s^{-1} later on. Residual currents at the OM site exhibited a two-layer positive circulation during upwelling wind forcing for the periods 19–21 August and 24–30 August (Figure 2b). The

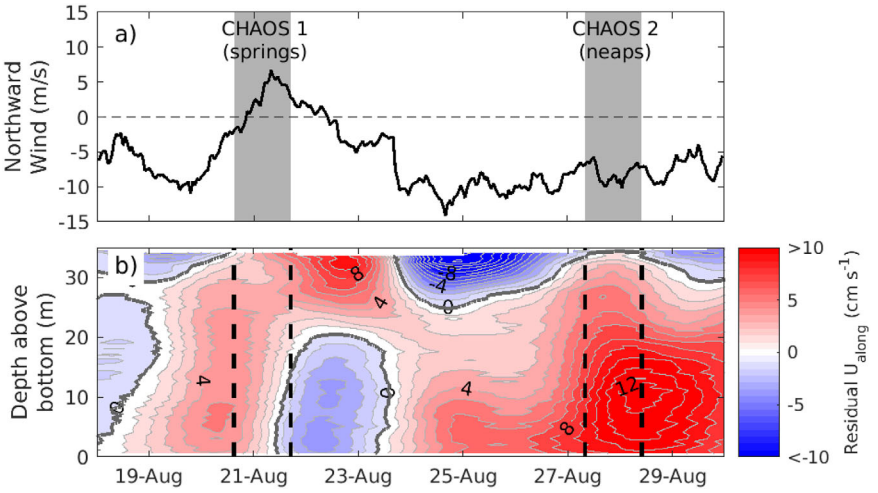

Figure 2. (a) Northward component of the wind speed (m s^{-1}) recorded at the Silleiro buoy (42.12 °N-9.43 °W) for a 12-day period (18–30 August 2013) spanning the two intensive samplings (indicated by the gray shading). (b) Along-Ría residual current velocity derived from moored ADCP measurements at the OM location for the same period. Isolines separate 1 m s^{-1} levels, the thick line represents the zero velocity isoline. Velocities are defined positive to the northeast (into the Ría). Vertical dashed lines indicate the periods of intensive observations.

Ría responded with an inversion of the circulation pattern to the relaxation-downwelling wind event (22–23 August). The response in the currents lagged the wind forcing by about 23 hours, which is longer than the local inertial period (17.3 h), indicating shelf-scale rotatory adjustment of the circulation to the changing winds.

The CHAOS 1-springs cruise coincided with the event of relaxation of upwelling-favorable winds. Equatorward upwelling-favorable winds started to weaken one day before, and reversed to northward about midnight on 20 August, while we were at sea (Figures 2a and 3a). In contrast, winds were upwelling-favorable and even strengthened during the central hours of the CHAOS 2-neaps cruise (Figure 3e). During both cruises, the water column exhibited thermal stratification, with temperatures $\leq$ 13 °C in the lower layers resulting from the penetration of upwelled cold oceanic central water, and warmer surface resulting from solar heating (15-16 °C) (Figure 3b,f). Due to the longer-lasting and more intense upwelling, the penetration of cold oceanic waters reached shallower depths during CHAOS 2 (20–30 m) compared to CHAOS 1 ($>$ 30 m), and surface temperatures were lower ($\lesssim$15 °C) during the neap tides cruise. As a consequence, subsurface thermal stratification at 7–9 m was more intense during CHAOS 1 and stratification close to the 13 °C isotherm was stronger during CHAOS 2. Haline stratification was weak and salinity values close to the ENACW salinity ($\sim$35.8) were observed during both cruises (Figure 3c,g), suggesting very little freshwater influence. The potential density anomaly (σ_θ) distribution showed permanent stable density stratification during both cruises, and a surface-to-bottom density difference of $\Delta\sigma_\theta$=0.71 kg m^{-3} and 0.52 kg m^{-3} for CHAOS 1 and 2, respectively. This indicates an overall stronger stratification during the spring-tides cruise (Figure 3d and 3h).

Current velocities exhibited a semidiurnal tidal cycle in both components, but with larger amplitudes in the along-Ría axis (Figure 4). Maximum inflow (29 cm s^{-1}) and outflow ($-$37 cm s^{-1}) velocities in this direction were higher during spring tides, compared to neap tides ($\pm$25 cm s^{-1}). The current profiles exhibited significant vertical structure in both situations. Outflow along the Ría during the ebb took place preferentially in the upper water column during both cruises (Figures 4a and 4b). Positive along-Ría currents during the flood showed, in general, an inverse structure, with maximum speeds near bed and decreasing toward the surface. This pattern was more pronounced during CHAOS 2 (Figure 4b).

3.2. Tidal Cycles of Turbulent Dissipation: Characteristics

Microstructure turbulence data revealed significant variability of the internal dissipation rates of TKE (ε) over the tidal cycles. A pronounced tidal cycle of ε was observed during CHAOS 1, with ε varying by about two orders of magnitude in mid-water (Figure 5a). During the ebbs, a patch of enhanced values of ε

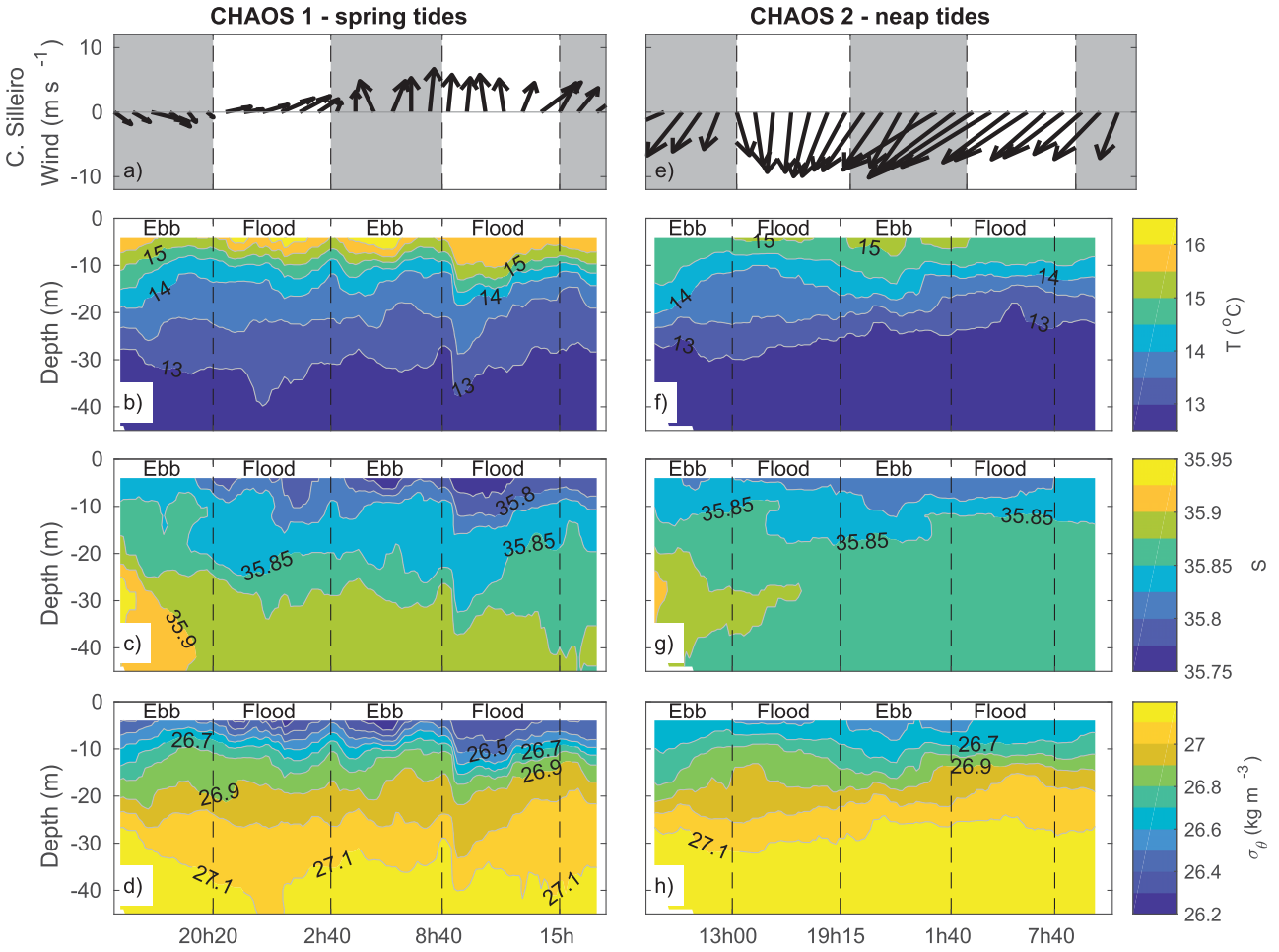

Figure 3. Evolution of the (a,e) wind vector (m s^{-1}) recorded at the Silleiro buoy (Remote shelf wind) (42.12 °N-9.43 °W), and the vertical distribution of (b,f) temperature (T, °C), (c,g) salinity (S), and (d,h) potential density anomaly (σ_θ, kg m^{-3}) during the two intensive sampling periods at outer Ría de Vigo: CHAOS 1 - Spring tides (20–21 August 2013) and CHAOS 2 - Neap tides (27–28 August 2013).

(10^{-6} W kg^{-1}) developed from the subsurface, 2 hours after high water, occupied almost the full water column some 2 hours later, and vanished within one hour after low water. During the floods, ε was reduced to about 10^{-8} W kg^{-1} in the central portion of the water column (15–30 m), but it remained generally higher ($\gtrsim 10^{-7}$ W kg^{-1}) in the upper 12 m. The ε variability was less pronounced during CHAOS 2 (Figure 5e). Dissipation rates were enhanced ($>1\times10^{-6}$ W kg^{-1}) in the upper 10–15 m from the mid first flood to the mid second ebb, and subsurface patches of relatively enhanced ε in mid-water were also observed during late ebbs to early floods. However, the vertical extent of the turbulent patches was restricted to depths between 10 and 25 m, and the maximum ε values ($<10^{-6}$ W kg^{-3}) were not as high as observed during CHAOS 1. A bottom boundary layer of elevated turbulence ($>10^{-7}$ W kg^{-3}) developed only during the floods during both cruises. Depth-integrated interior TKE dissipation rates (excluding the bottom boundary) were higher by a factor 1.2-2.5 during CHAOS 1 (4.7–6.5 mW m^{-2}) compared to CHAOS 2 (and 1.9–5.7 mW m^{-2}), depending on whether the upper boundary layer (calculated as the depth where ε drops below $<10^{-6}$ W kg^{-1}) was included in the calculation. Dissipation observed within this layer was likely driven by interior processes (see below), but we cannot discard some influence of direct wind or wave mixing.

The buoyancy Reynolds number (Re_b) followed the ε distribution in surface and subsurface waters, being $Re_b \gtrsim 10^2 - 10^3$ within the regions and periods of enhanced dissipation (i.e. during the ebbs of CHAOS 1 and late ebbs of CHAOS 2 in mid-water, and during the floods of CHAOS 1 and the late-first flood to early-second ebb of CHAOS 2 in the upper layers) (Figures 5b and 5f). Concomitantly, the Thorpe length-scale (L_T), describing the size of the turbulent overturns, adopted relatively larger values ($L_T \gtrsim 10^{-0.5} \simeq 0.3$ m)

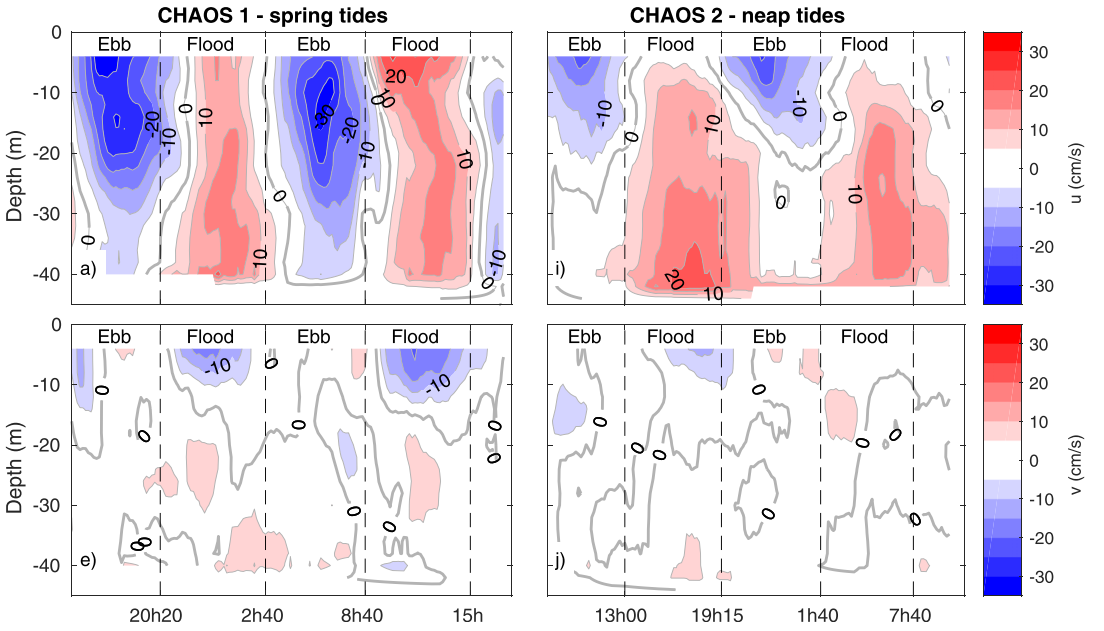

Figure 4. Evolution of the vmADCP derived currents (a,c) along (u, cm s^{-1}) and (d,e) accros (u, cm s^{-1}) the Ría axis during the two intensive sampling periods at outer Ría de Vigo: CHAOS 1 - Spring tides (20–21 August 2013) and CHAOS 2 - Neap tides (27–28 August 2013).

compared to the background ($<$ 0.3 m) (Figures 5c and 5g). Furthermore, the turbulent Froude number, representing the ratio of the buoyancy length scale to the overturning eddy size, was close to one (Figures 5d and 5h). These results indicate that, during the periods of enhanced dissipation, turbulence was energetic ($Re_b > 10^2$), presenting relatively large overturns in equilibrium with stratification ($Fr_T \sim 1$). In turn, during the periods of reduced mixing, turbulence transited to a buoyancy-controlled regime ($Re_b < 100$), and the turbulent eddies were progressively suppressed by stratification ($Fr_T < 1$).

Re_b exhibited values of $10^3 - 10^4$, indicative of the energetic regime of turbulence, in the bottom boundary layers during both cruises (Figure 5b,f). During CHAOS 1, values of $Re_b > 10^4$ coincided with enhanced dissipation near the bottom (Figure 5b). L_T was ~1 m in the bottom layers during the whole CHAOS 1 sampling (Figure 5c). The tidal cycle was less evident in L_T compared to ε and Re_b, and significant overturns were found even when dissipation was minimum, e.g. during the second ebb. However, the turbulent Froude number (Fr_T) was large ($>$ 2) during the floods of CHAOS 1, and $<$ 1 during the ebbs, indicating that the observed overturns were likely decaying (Figure 5d). During CHAOS 2, the area of large Re_b ($>10^3$) and Fr_T ($>$1–2) grew from a depth of 40 m to 30 m after the first flood, due to the progression of the upwelled waters and consequent reduction of near-bottom stratification (Figures 5f and 5h). Higher values of Re_b ($>10^4$) and larger overturns ($L_T > 2$) were found during the second flood, when dissipation was also enhanced (Figures 5f and 5g).

3.3. Tidal Cycles of Turbulent Dissipation: Drivers

In the previous section, we have shown the occurrence of significant tidal variations in different turbulence-related quantities during the CHAOS cruises. The overall increase of TKE dissipation observed in the bottom layers during the floods was likely related to the enhanced bottom friction, due to the larger near-bottom velocities observed for this period (15–20 cm s^{-1}), in comparison with the ebb (0–10 cm s^{-1}). However, enhanced ebb dissipation observed in mid-water seems to be disconnected from the direct action of bottom friction, as the patches of enhanced ε either grew from the pycnocline toward the bottom (CHAOS 1), or were completely isolated from it (CHAOS 2) (Figures 5a and 5e). The water column remained stably stratified during the entire tidal cycles, as observed in the σ_θ distributions (Figures 3d and 3h) and in the small size of the turbulent overturns ($<$ 1 m, Figures 5c and 5g). This suggests that the periods of enhanced turbulence were not produced by convective instabilities. Here, we describe the tidal variability of the Richardson number, shear and stratification to demonstrate that these variations in mid-water dissipation were due to shear instabilities of the mean flow.

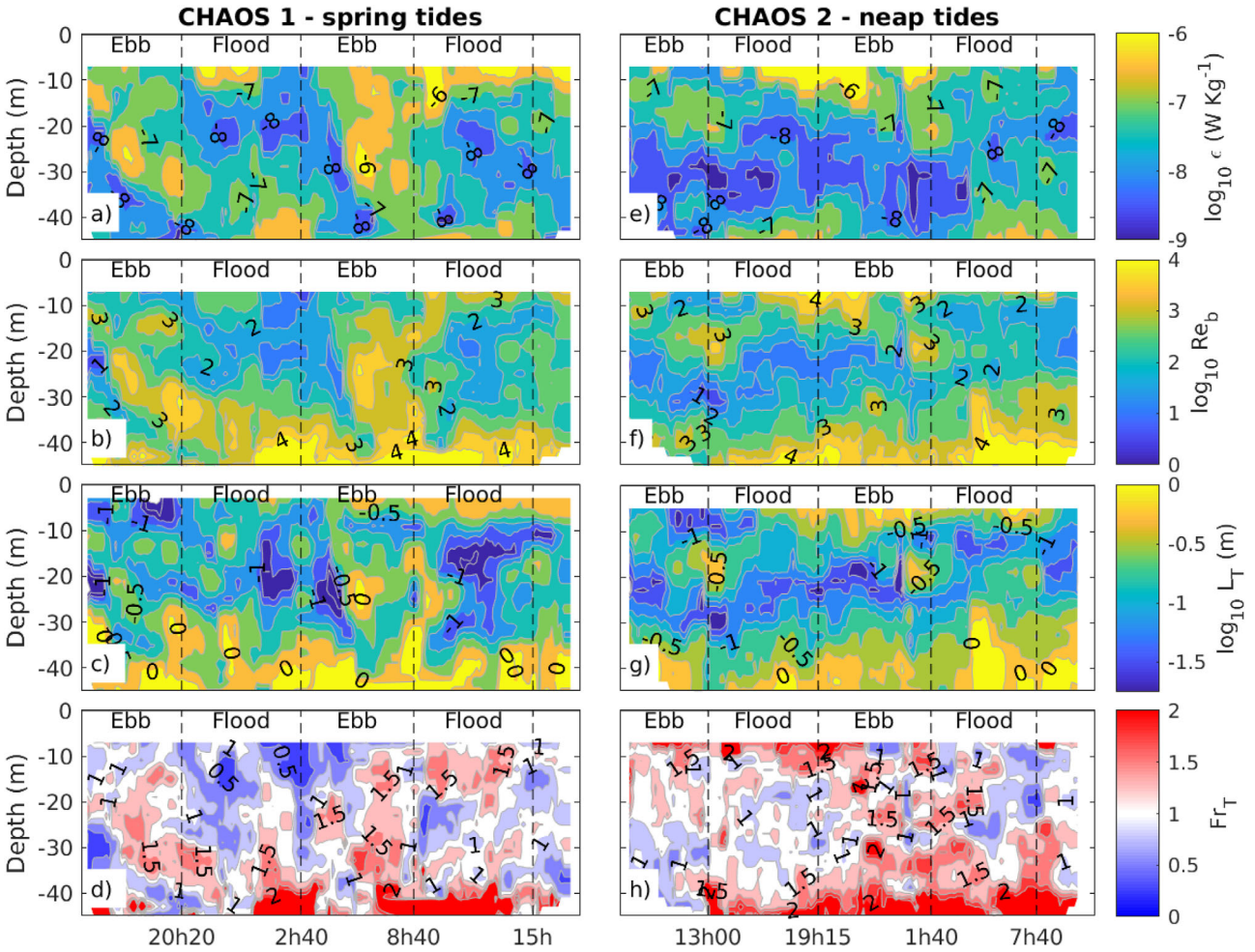

Figure 5. Evolution of the (a,e) MSS-observed dissipation rate of turbulent kinetic energy (ε, W kg^{-1}), (b,f) buoyancy Reynolds number ($Re_b = \varepsilon/\nu N^2$) and Thorpe length-scale (L_T, m), (c,g) and (d,h) turbulent Froude number ($Fr_T = (L_O/L_T)^{2/3}$) during the two intensive sampling periods at outer Ría de Vigo: CHAOS 1 - Spring tides (20–21 August 2013) and CHAOS 2 - Neap tides (27–28 August 2013).

The median value of the Richardson number was Ri ∼1 during both cruises, indicating a state of marginal stability. During the ebbs of CHAOS 1, values of $Ri^{-1} > 1$ reaching $Ri^{-1} > 4$ ($Ri < 0.25$) occasionally were observed from 15 m to 35 m, matching the high-dissipation patch (Figure 6a). During the second flood, high values of Ri^{-1} in subsurface waters were also coincident with enhanced dissipation. A similar co-evolution of high Ri^{-1} with high ε was observed during CHAOS 2, at least in the upper 20 m (Figure 6d). A deeper layer of high Ri^{-1} was apparent during this cruise, with no associated dissipation. Although subcritical values of Ri (< 0.25) were only reached sporadically, the strong coincidence of the ε and Ri distributions is consistent with shear instability being the driver of the observed tidal cycles of turbulent dissipation. We attribute the lack of observations of subcritical Ri values to the fact that the sh^2 and N^2 were derived from different instruments, and that high-frequency variability was smoothed out by bin-averaging with a 1-hour window.

According to the Ri definition, the triggering of shear instability is controlled by the balance between turbulence production by shear and suppression by stratification. The distribution of the buoyancy frequency (N) showed relatively weak variability through the tidal cycle during CHAOS 1, with a main subsurface pycnocline of $N \sim 12$ cph at 7–9 m, and weaker though significant stratification (4–8 cph) down to 35 m (Figure 6b). The evolution of the Richardson number was mostly controlled by the more variable distribution of shear (sh) (Figure 6c). During CHAOS 2 two pycnoclines were observed, one located close to the surface associated with solar heating (8–12 cph), and a weaker one close to 20 m associated with the 13 °C isotherm (5–9 cph). The N distribution was more variable during this cruise and both pycnoclines merged

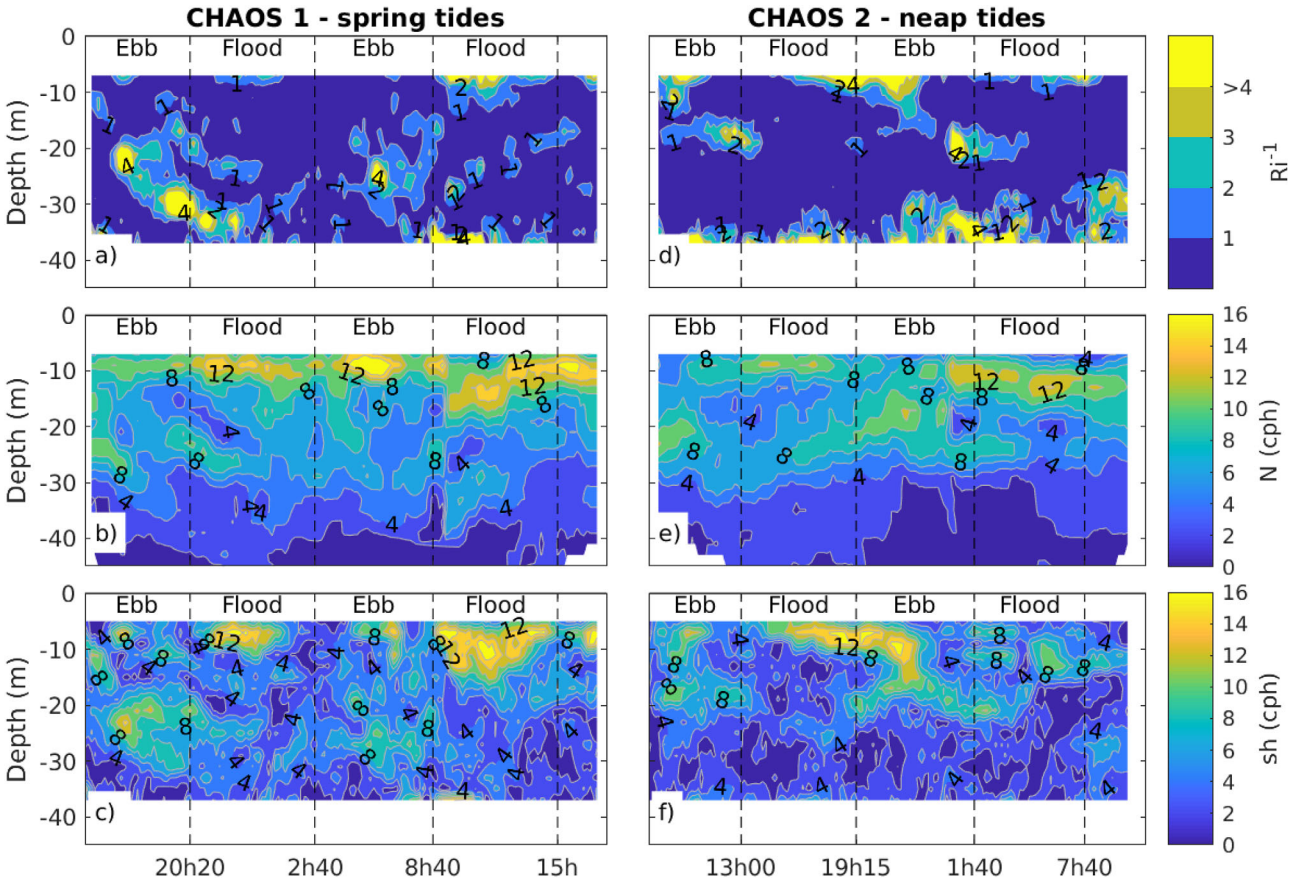

Figure 6. Evolution of the (a,d) inverse gradient Richardson number ($Ri^{-1} = sh^2/N^2$), (b,e) buoyancy frequency (N, cph) and (c,f) shear (sh, cph) during the two intensive sampling periods at outer Ría de Vigo: CHAOS 1 - Spring tides (20–21 August 2013) and CHAOS 2 - Neap tides (27–28 August 2013).

together during some parts of the tidal cycle, particularly during the ebbs (Figure 6e). During this cruise, the regions of enhanced shear were clearly associated with the pycnoclines (Figure 6f). Despite this coincidence, shear was strong enough to overcome stratification and control the distribution of Ri. In the following section we examine the velocity components to diagnose the drivers of the shear distribution.

3.4. The Tidal Cycles of Shear: Upwelling-Tide Interactions

The residual currents in the along-Ría axis (u^R) exhibited a two-layer upwelling circulation at the beginning of the CHAOS 1 cruise, with outflow above 25 m and maximum at the surface ($\sim$10 cm s^{-1}), and inflow ($\leq$ 6 cm s^{-1}) below (Figure 7a). As a result of shifting winds, both inflow and outflow weakened, the outflow deepened and a subsurface inflow ($\leq$ 6 cm s^{-1}) developed along the CHAOS 1 sampling. The rapid current reversal of the upper layers is indicative of a response to the local winds, rather than a shelf-scale adjustment to the remote winds (Gilcoto et al., 2017). Although not shown here, local winds measured at the Cíes Buoy (Figure 1) and remote winds (Figure 3a) followed a similar evolution. A well-developed upwelling circulation was observed during CHAOS 2, with outflow concentrated in the upper 10 m. The intensity of the shallow outflow reduced from 8 to 2 cm s^{-1}, as deep inflow strengthened slightly to a maximum value of 10 cm s^{-1} by the end of the cruise (Figure 7g). The residual currents were more energetic during CHAOS 2-neaps compared to CHAOS 1-springs, with a depth-integrated kinetic energy (KE) of 90.7 J m^{-2} and 52.9 J m^{-2}, respectively.

The maximum amplitude of the semidiurnal tide in the along-Ría axis (u^{M_2}) was larger during spring tides (21 cm s^{-1}, Figure 7b) compared to neap tides (13 cm s^{-1}, Figure 7h), and the KE of the depth-averaged currents was also 3.5-fold higher during CHAOS 1 (269.6 J m^{-2}) compared to CHAOS 2 (75.9 J m^{-2}). During CHAOS 1 (and CHAOS 2), tidal currents exhibited vertical structure, with maximum amplitude of 21.1 cm s^{-1} (12.7 cm s^{-1}) at the base of the pycnocline, reduced toward the surface and bottom, reaching a minimum

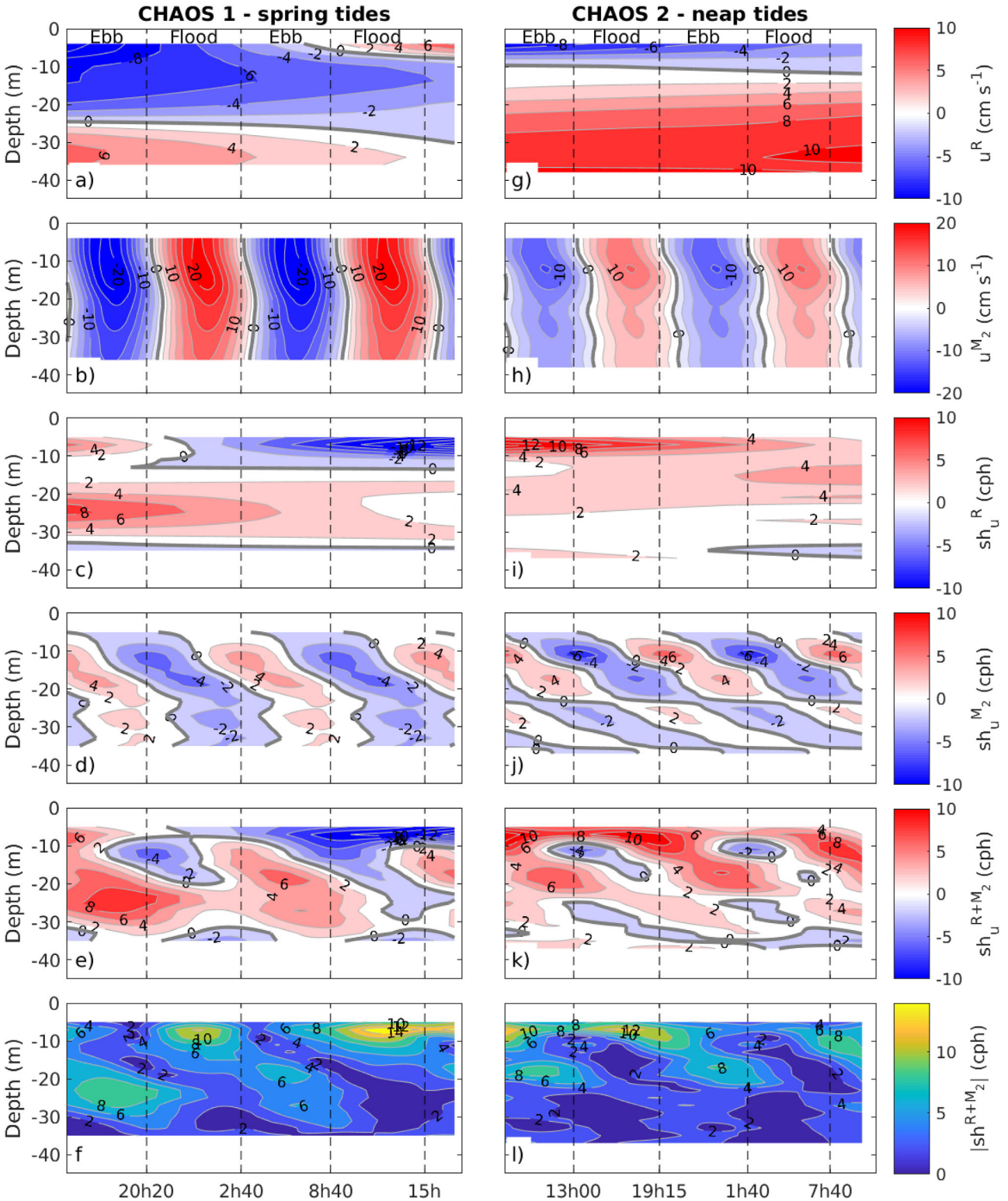

Figure 7. Currents and shear calculated in the along-Ría axis during the two intensive sampling periods at outer Ría de Vigo: CHAOS 1 - Spring tides (20–21 August 2013) and CHAOS 2 - Neap tides (27–28 August 2013). Panels (a,g) and (b,h) represent the evolution of the residual (u^R, cm s^{-1}) and tidal currents (u^{M_2}, cm s^{-1}), respectively. Panels (c,i) and (d,j) represent the shear of the residual (sh_u^R, cph) and tidal currents, ($sh_u^{M_2}$, cph), respectively, and panels (e,k) the superposition of both residual and tidal shear ($sh_u^{R+M_2}$, cph). Panels (f,l) represent the magnitude, $|sh^{R+M_2}| = \sqrt{(sh_u^{R+M_2})^2 + (sh_v^{R+M_2})^2}$, of the total (tidal + residual) shear.

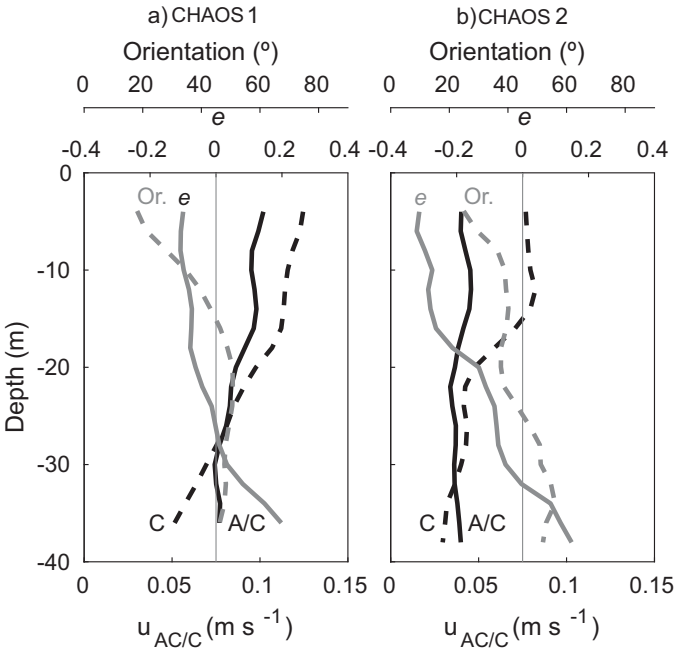

Figure 8. Characteristics of the M_2 tidal ellipses during the two intensive sampling periods at outer Ría de Vigo: (a) CHAOS 1 - Spring tides (20–21 August 2013) and (b) CHAOS 2 - Neap tides (27–28 August 2013). The black solid and dashed lines represent the amplitude of the anticlockwise (u_{AC}) and clockwise (u_C) components, respectively; and the gray solid and dashed lines represent the ellipticity (e) and orientation of the ellipses (° N of E). The gray thin vertical line represents $e = 0$ and the orientation of the Ría axis (45° N of E).

value of 12.4 cm s^{-1} (6.9 cm s^{-1}) at 38 m. Tidal ellipses showed vertically variable ellipticity (e), shifting from positive values (indicative of anticlockwise rotation) below 30 m, to negative values (clockwise rotation) toward the surface, as a consequence of the larger vertical variation of the clockwise vector amplitude (Figure 8).

These results are consistent with theory and observations in coastal areas (Howarth, 1998; Palmer, 2010; Prandle, 1982; Souza & Simpson, 1996), which demonstrated that the bottom friction in the presence of stratification induces a modification of the tidal ellipses with depth, due to the different thickness of the Ekman layer for the clockwise and anti-clockwise rotating vectors. An empirical criterion for significant tidal ellipse deformation to occur has been established based on the bulk Richardson number $\mathrm{Ri}_o = gh\Delta\rho/\rho U^2 > 0.5$, where U is the amplitude of the tidal current (Soulsby, 1983). This condition was largely met during both CHAOS 1 ($\mathrm{Ri}_o \sim 6.1$) and CHAOS 2 cruises ($\mathrm{Ri}_o \sim 13$). Interestingly, our data showed an inflection point of the clockwise amplitude associated with the base of the pycnocline during both cruises, but the shear was distributed differently: during CHAOS 2 it was more concentrated around 12–20 m, and during CHAOS 1 was more spread from 17 to 35 m (Figure 8). This was likely related to the less stratified deeper layer during CHAOS 2, and the sharper interface of the 13 °C upwelled water, due to strengthened upwelling. This result suggests that the vertical structure of the tidal currents was controlled indirectly through stratification by the stage of development of the upwelling event.

Throughout the spring tides cruise the vertical shear of the along-Ría residual currents- (sh_u^R, i.e. the vertical derivative of the along-Ría residual velocity, u^R) was positive between 12 and 34 m (Figure 7c). In the upper 12 m, sh_u^R changed from positive to strongly negative as surface inflow driven by local winds developed. Along-Ría tidal shear ($sh_u^{M_2}$) varied through the tidal cycle with 6 h phase-lag across the pycnocline between 4 and 20 m (Figure 7d). It added constructively to the upwelling shear during the ebbs (and destructively during the floods) at mid-water between 12 and 35 m, resulting in maximum and positive total along-Ría shear (sh^{R+M_2}) for this period and depth range (Figure 7e). During the second flood, $sh_u^{M_2}$ and sh_u^R were both negative around the pycnocline, resulting in enhanced negative total shear ($sh_u^{R+M_2}$). During both floods, the tidal ($sh_v^{M_2}$, Figure 9d) and residual shear (sh_v^R, Figure 9c) terms in the across Ría axis interfered constructively. As a consequence of these interference patterns, the vector module of along and across-Ría tidal and upwelling shears ($|sh^{R+M_2}|$) was enhanced during the ebbs at the interface between the upwelled and surface waters, i.e. 12 to 35 m, and during the floods at the subsurface thermocline (Figure 7f).

During the neap tides cruise sh_u^R was positive throughout the water column, but took higher values in the upper 10 m (Figure 7i). $sh_u^{M_2}$ was also positive around high water in the upper 12 m, and during the ebbs and early floods between 12 and 25 m (Figure 7j), interfering constructively with the residual shear (Figure 7k). The interference was destructive at low water in the upper 12 m and during the floods at 12–20 m. Thus, similar to CHAOS 1, $|sh^{R+M_2}|$ was enhanced during the ebbs at the limit of the upwelled waters, between 12 and 25 m (Figure 7l). The variability of $|sh^{R+M_2}|$ at the subsurface thermocline (upper 10 meters) was also the result of these interactions. It was higher during the first flood and the early second ebb (Figure 7k), when the $sh_u^{M_2}$ and $sh_u^{M_2}$ were positive (Figure 7i,j), before surface outflow weakened (Figure 7g), reducing $sh_u^{M_2}$ (Figure 7i).

This analysis revealed that the interactions of semidiurnal and residual currents were the main drivers of shear variability, as the shear patterns emerging from these interactions (Figure 7f,l) strongly coincided with direct shear observations (Figures 6c and 6f). Although the depth-averaged squared-shear of the residual circulation (0.51 s^{-2} for CHAOS 1 and 0.44 s^{-2} for CHAOS 2) was stronger than the shear produced by the tidal currents (0.36 s^{-2} for CHAOS 1 and 0.23 s^{-2} for CHAOS 2), the tide controlled the timing of occurrence of the enhanced internal shear. In this way, a tidal cycle of turbulent dissipation at mid depths emerged

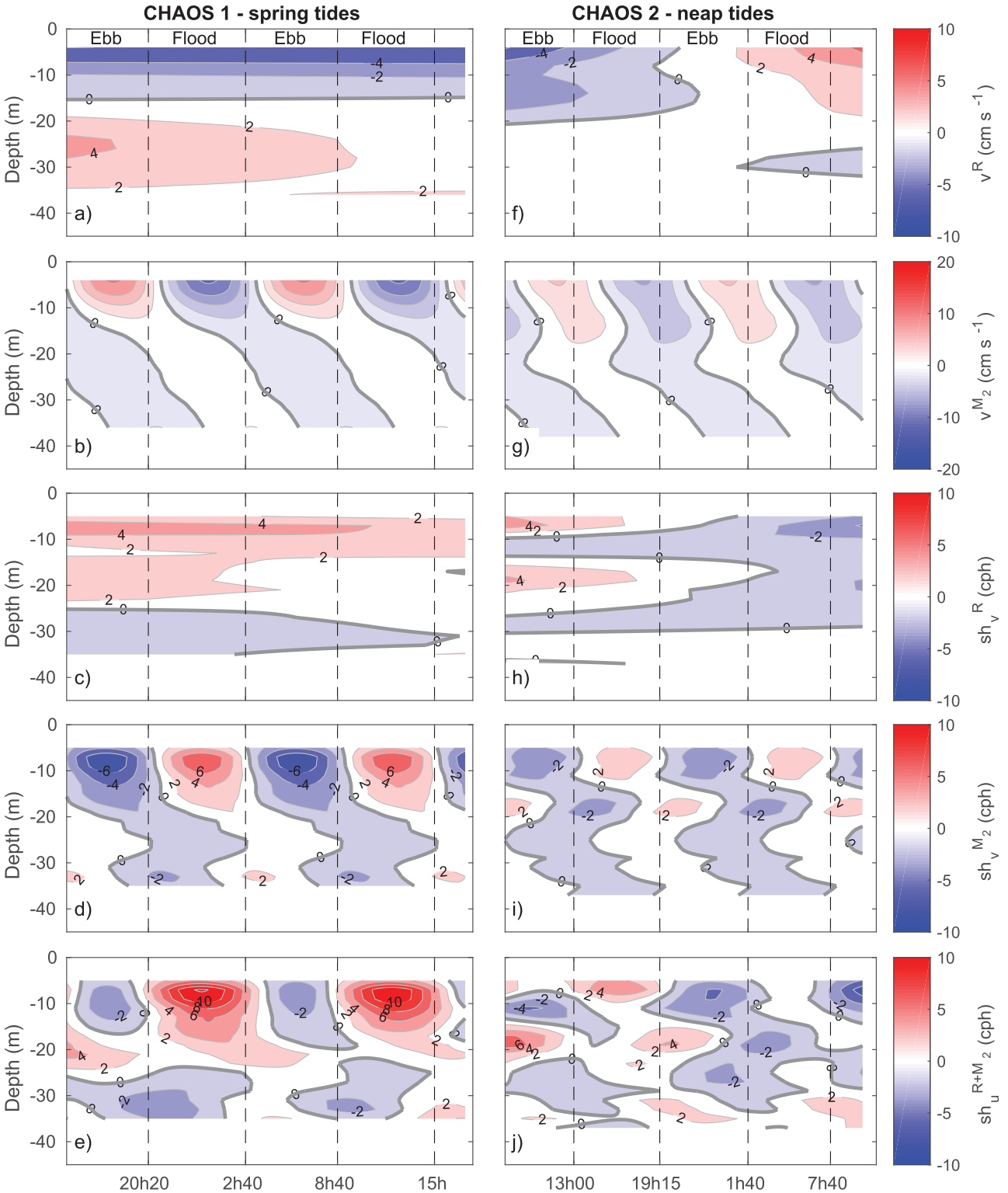

Figure 9. Currents and shear calculated in the across-Ría axis during the two intensive sampling periods at outer Ría de Vigo: CHAOS 1 - Spring tides (20–21 August 2013) and CHAOS 2 - Neap tides (27–28 August 2013). Panels (a,f) and (b,g) represent the evolution of the residual (u^R, cm s^{-1}) and tidal currents (u^{M_2}, cm s^{-1}), respectively. Panels (c-h) and (d,i) represent the shear of the residual (sh_u^R, cph) and tidal currents, ($sh_u^{M_2}$, cph), respectively, and panels (e, j) the superposition of both residual and tidal shear ($sh_u^R + sh_u^{M_2}$, cph).

with enhanced interfacial dissipation during the ebbs, when the tidal and residual upwelling shear added constructively. On the contrary, bottom dissipation was enhanced during the floods (Figure 5a,e) when the near-bed currents were stronger due to the superposition of subtidal (Figure 7a,g) and tidal flows (Figures 7b and 7h), increasing the bed stress. This effect was more noticeably during CHAOS 2, when the near-bed subtidal currents were stronger.

4. Discussion

4.1. The Tidal Cycle of Shear-Driven Turbulent Mixing

Our microstructure and currents observations carried out in the Ría de Vigo during the 2013 summer-upwelling season, revealed a semidiurnal cycle of turbulent dissipation characterized by enhanced mid-water dissipation during the ebbs, at the interface between the upwelled and surface waters, driven by the interference of subtidal and tidal shears. The vertical distribution of shear was controlled by the intensity of upwelling directly and indirectly, through the deformation of tidal ellipses by stratification. The overall larger values of depth-integrated dissipation during the CHAOS 1 are likely related to the less sharp interface of the upwelled waters, due to the upwelling relaxation occurring during this period. Thus, our analysis suggests that the upwelling modulates the tidal cycle of turbulent dissipation in the Ría de Vigo.

Unlike for other partially mixed estuaries (Stacey & Ralston, 2005; Stacey et al., 1999), we found that a significant fraction of the turbulent dissipation in the Ría occurred away from the direct influence of bottom friction. The described tidal cycle of interior turbulent dissipation was opposed to that expected to be induced by tidal straining (Rippeth et al., 2001; Simpson et al., 2005), which would result from convective-mixing caused by the advection of dense over light waters during the floods. The water column remained statically stable during the two sampled tidal cycles in the Ría de Vigo, and we found no evidence of convection occurring during these periods. Although density straining seems to play a minor role in the cycle of turbulent dissipation, its influence on stratification is examined in the next section. On the other hand, the described tidal cycle of dissipation is similar to that found in many salt wedge (Geyer & Farmer, 1989; Kay & Jay, 2003b; Macdonald & Horner-Devine, 2008; Partch & Smith, 1978; Ralston et al., 2010) and also partially mixed estuaries (Peters, 1997; Peters & Bokhorst, 2000), where enhanced shear-driven interfacial mixing was also documented during the ebb tides. Jay and Musiak [1996] and Kay and Jay [2003b] suggested that this pattern was driven by the combined actions of the tidal shear and the shear of the subtidal fluvial batropic (and baroclinic) circulation.

The Ría de Vigo differs in its morphology and dynamics from those estuaries where similar cycles have been described. The Ría is generally much deeper ($\sim$40 m in the central channel, vs. typically $\lesssim$ 15 m), less influenced by freshwater inputs in summer, when its subtidal circulation is not directly driven by river discharge events or horizontal density gradients, but connected to the shelf dynamics through wind-driven coastal upwelling (Souto et al., 2003; Gilcoto et al., 2007) (see Figure 2). While in salt wedge estuaries shear-driven turbulence occurs at the salt wedge interface, in the Ría the turbulence emerges at the interface of the upwelled waters. Furthermore, other than to remote winds over the shelf, the Ría responds to local wind forcing, and this response is faster than to shelf winds, although the two scales of wind forcing tend to reinforce each other due to the orientation of the Ría (Gilcoto et al., 2017). This fast response of the upper layers of the Ría to the local winds was observed during the second part of CHAOS 1 (Figure 7a), producing additional shear (Figures 7c and 7e) and enhanced dissipation (Figure 5a). Similar effects of local wind forcing on interior shear production and mixing have been predicted in a model study of an idealized estuary (Chen & Sanford, 2009).

We can not discard that other mechanisms, such as internal waves, could have contributed to the observed shear and turbulence patterns, as it has been suggested in previous studies. In fact, the analysis of Synthetic Aperture Radar (SAR) images acquired during the summer months of 2008–2011 in the shelf off the Ría de Vigo revealed that non-linear internal waves (NIWs) were more energetic during spring tides (Villamaña et al., 2017). Although the presence of non-linear internal waves was not evident during the CHAOS cruises in the southern mouth of the Ría, they were apparent in the WireWalker (WW) mooring located 6.6 km offshore (Figure 10). This fact suggests that NIWs probably attenuate within the outer Ría, as it has been suggested in previous studies (Varela et al., 2005). By using the Korteweg-de-Vries (KdV) theory (Jeans & Sherwin, 2001; Michallet & Barthelemy, 1998) we estimated an upper limit for the dissipation rate of NIWs.

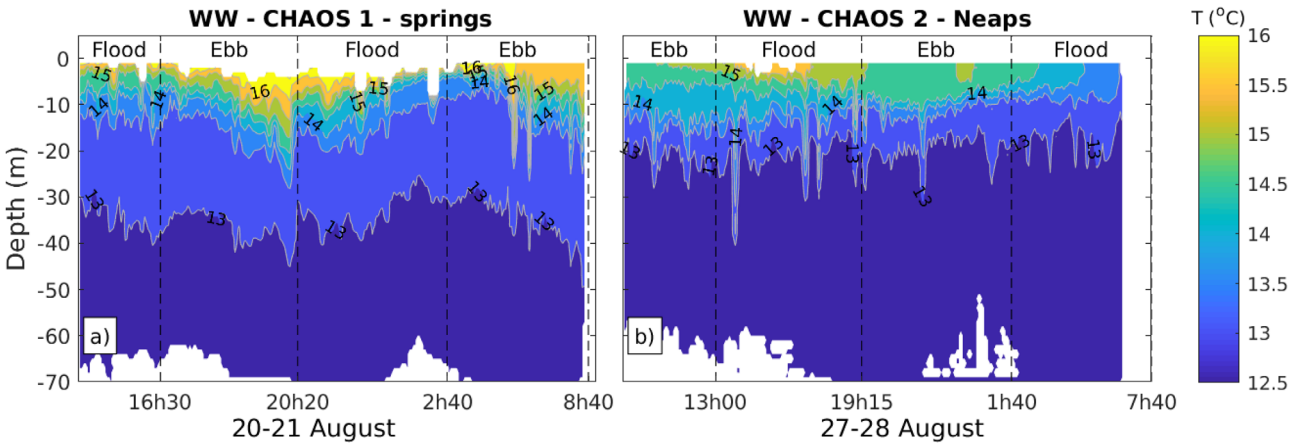

Figure 10. Temperature time-series data collected with a WireWalker mounted CTD at 42.13 °N-8.95 °W (Figure 1) for a) spring (CHAOS 1, 20–21 August 2013) and b) neap (CHAOS 2, 27–28 August 2013) tides.

The energy flux driven by NIW propagation is the product of their energy content (PE + KE) and their group velocity (see Methods). The potential energy of the high frequency (> 1 cph) internal waves, obtained from the integration of density fluctuations power spectrum at the WW site, was 8 J m^{-2} and 19 J m^{-2}, for CHAOS 1 and CHAOS 2, respectively. According to the KdV theory (Eqs. 5–6) and the characteristics of the observed NIWs, we predicted group velocities of c=0.36 m s^{-1} and 0.33 m s^{-1} for CHAOS 1 and CHAOS 2. With this, energy fluxes were 5.8 W m^{-1} and 12.5 W m^{-1}, respectively. If we assumed that the waves dissipated within the distance between the WW mooring and the main sampling site (MY, Figure 1), the averaged dissipation rates would be 0.87 W m^{-2} and 1.90 W m^{-2}, for CHAOS 1 and CHAOS 2, respectively. Therefore the dissipation of the energy carried out by NIWs would represent a modest but non negligible (20−33%) fraction of the dissipation observed during the CHAOS cruises.

4.2. Buoyancy Balance: Mixing Versus Straining and Advection

One of the main implications of the tidal cycle of turbulent dissipation observed during the CHAOS cruises is that it can impact the buoyancy balance (Equation 7), and potentially induce tidal asymmetries in stratification. The buoyancy frequency (N) exhibited some variability during the CHAOS 1 and CHAOS 2 cruises, but a distinct semidiurnal cycle, as observed for turbulent dissipation, was not evident and the water column remained stably stratified during the entire tidal cycles. With a simple two-layer model approach, we inferred the horizontal density gradients at our sampling location, and evaluated the contribution of turbulent mixing, straining (Simpson et al., 1990) and advection (Giddings et al., 2011) to the observed variability in stratification (see Methods). Despite the model simplifications, it was able to reproduce the general patterns of stratification observed during both cruises (Figures 11a and 11d). The diagnosed density gradients in the along-Ría direction changed signs during both cruises, and were in general weaker than in the perpendicular direction (Figures 11b and 11e). During the first half of the CHAOS 1 cruise, advection of N^2 in the along-Ría direction dominated the N^2 variability (Figure 11c), while the increase in stratification during the second flood was co-dominated by advection and straining in the perpendicular direction. During CHAOS 2, the two advective terms (Figure 11f) were dominant, particularly during the first 12 hours. The diffusive term was of secondary relevance for the local variations of stratification during both cruises.

The variations of stratification during the CHAOS cruises were different from those expected as a result of tidal (Simpson et al., 1990) or wind-induced straining (Scully et al., 2005; Chen & Sanford, 2009). As density typically decreases toward the head of the estuary, tidal straining increases stratification during the ebbs and decreases it during the floods (Simpson et al., 1990). Similarly, along-channel straining by down-estuary (up-estuary) winds tend to increase (reduce) stratification (Scully et al., 2005; Chen & Sanford, 2009; Xie & Li, 2018). Due to the fact that the vertical shear of the subtidal currents was in general larger than that of tidal currents, straining was dominated by the subtidal, instead of the tidal circulation, and for this reason a continuous increase of stratification would be expected. However, this was not the case and this unusual behavior of the Ría could be attributed to several particular characteristics. First, the advective terms were as relevant as the

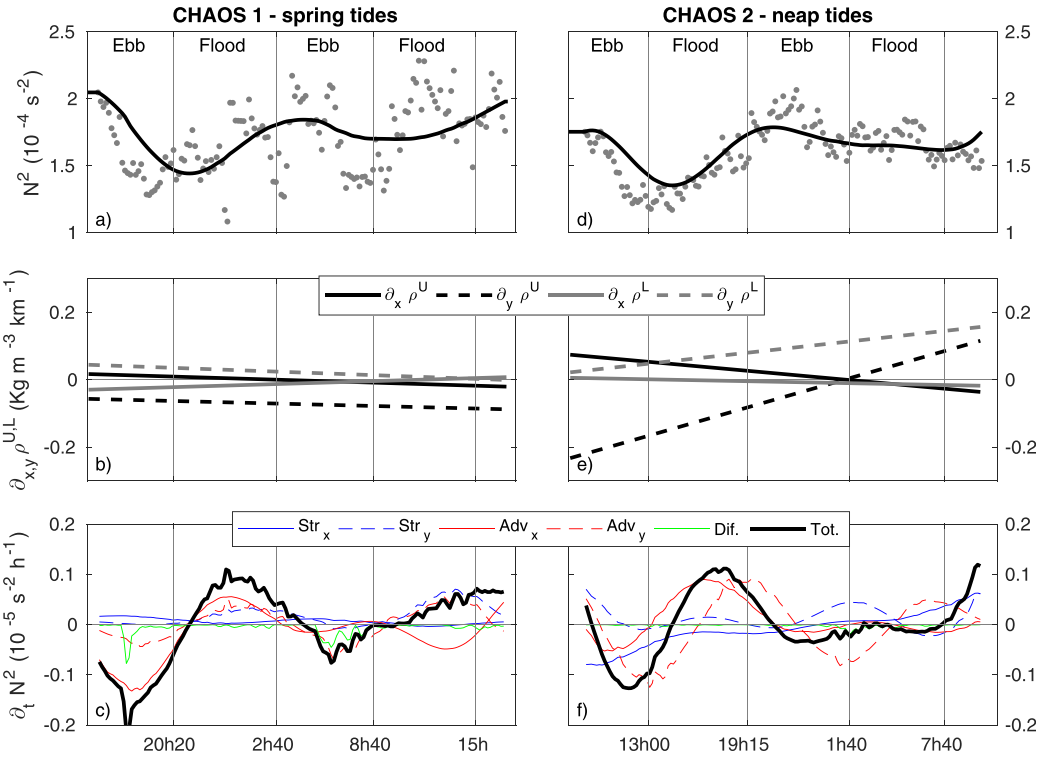

Figure 11. (a,d) Temporal evolution of the stratification (N^2) between the upper and lower layers of the two layer model. Gray dots and the thick black line represent the N^2 value derived directly from observations and from the straining-advection-mixing balance (equarion (7)). (b,e) Horizontal density gradients in the along (x) and across (y) Ría directions for the upper (U) and lower (L) layers ($\partial_{x,y}\rho^{U,L}$). (c,f) Time-derivative of N^2 ($\partial_t N^2$). The contribution of straining (blue), advection (red) and diffusion (green) in the x-along (solid) and y-across (dashed) directions to the total (thick, black) time-derivative are represented.

straining terms for the stratification balance. A similar situation was noted by Giddings et al. (2011) in a salt wedge estuary. Second, the horizontal density gradients diagnosed by the two-layer model were more complex than the depth-uniform density increase toward the ocean usually assumed for estuaries (Figures 11b ans 11e). Finally, our model suggested an important contribution of the straining and advection terms in across-Ría axis. This is in good agreement with previous field surveys in the Ría de Vigo that reported significant thermohaline gradients in the across-Ría direction (Barton et al., 2015; Piedracoba, 2005).

There are also several factors that could explain the atypical density gradients diagnosed for the along-Ría direction during the CHAOS cruises. First, with averaged tidal currents of the order of 0.1-0.2 m s^{-1} and of $\sim$ 0.07 m s^{-1} in the along and across Ría directions, respectively; tidal excursions were of about 3 km and 150 m, representing 10% and 1% of the Ría dimensions. Hence, the diagnosed density gradients were likely representative of the local rather than basin-scale variability. Second, there is little riverine discharge in the Ría during the summer-upwelling season (Ríos et al., 1992), such that the influence of the local rivers might be restricted to the inner-most Ría (Barton et al., 2015; Villacieros-Robineau et al., 2013), as suggested by the overall high salinity levels found during the CHAOS cruises. The density gradient along the Ría depends rather on a balance between cooling due to the upwelling of the central water within the Ría and solar heating. Thus, these gradients would evolve as upwelling progresses or relaxes, as found in the model approach. Furthermore, the most important source of freshwater in the Rías Baixas area is the river Miño, situated 30 km south of the Ría de Vigo. It is not unusual that southerly winds spread the Miño river buoyant plume northward, and that the Ekman transport piles up light water against the continent and carries it into the Rías, creating an inverse salinity gradient (Alvarez et al., 2006; Mouriño & Fraga, 1982; Sousa et al., 2014). Therefore, the sharp increase of stratification associated with the presence of relatively fresher water at the surface, and inflowing currents during the second flood of CHAOS 1 (Figures 3c and 11a), could have been influenced by the advection of shelf surface light water.

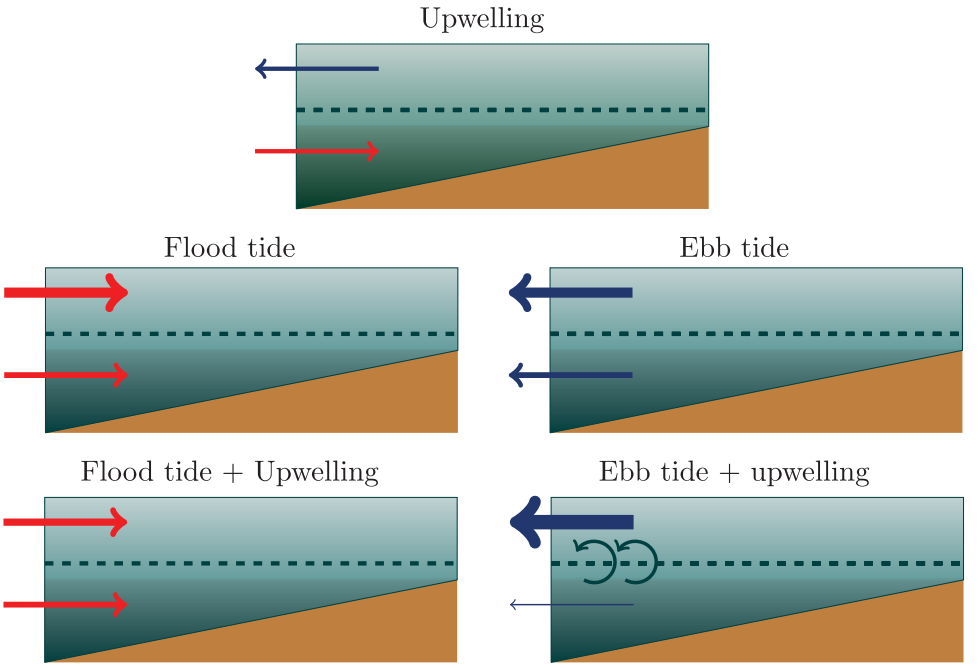

Figure 12. Schematic representation of the mechanism responsible for the tidal asymmetry in shear-instability mixing in the Ría de Vigo under upwelling stratified conditions. Shear at the interface separating the upper and the lower layers is due to both bi-directional upwelling circulation and tidal currents. As a result of upwelling winds over the shelf, cold oceanic waters intrudes as a lower layer into the Ría, while the relatively warm waters inside the Ría flow as an upper layer toward the ocean. The so-induced vertical stratification decouples the tidal currents of the upper and lower layers, resulting in faster tidal currents in the upper layer. Total shear at the interface is thus enhanced during the ebbs, when tidal and upwelling shear add-up, and reduced during the floods, when they cancel mutually

5. Conclusions

By using two 25-hours cycles of intensive sampling of turbulence microstructure and currents in the Ría de Vigo (NW Spain) during spring and neap tides, we described a semidiurnal tidal cycle of interior turbulent dissipation resulting from the interplay of the bi-directional upwelling circulation and the tidal currents shear. Constructive interference occurring during the ebbs resulted in shear instability mixing at the interface of the upwelled waters, whereas destructive interference during the floods resulted in reduced mixing (see an schematic representation of the process in Figure 12). The upwelling conditions determined the shear and turbulence distribution directly, through bi-directional flow, and indirectly, by modifying stratification which, in turn, caused tidal ellipses deformation. Thus, the overall enhanced dissipation levels observed during spring tides are related to differences in the upwelling conditions, instead of variations in the tide intensity. Although the timing of the described cycle of interior dissipation is similar to that found in other partially mixed or salt wedge estuaries, its particularity resides on the major role played by the residual wind-driven upwelling circulation, which is described here for the first time.

This mechanism could have important implications for the functioning of other physical and biological processes, contributing to the dynamical balance, and participating in the transport of heat, dissolved substances, inorganic particles and organisms. In particular, it can act as a pathway for nutrient supply from upwelled nutrient-rich deep waters into the sunlit surface waters, which is relevant for upwelling ecosystems (Hales et al., 2005). In fact, diffusive nitrate fluxes due to the enhanced dissipation, as observed during CHAOS 1-springs, could be responsible for about half of the phytoplankton primary production estimated in this system during periods of upwelling relaxation-stratification (Villamaña et al., 2017). Interactions between upwelling circulation and tides, similar to those described here, could occur in other upwelling systems, particularly bays with a bi-directional response to the forcing winds, like the Gulf of Arauco (Valle-Levinson, 2003) and Concepción Bay (Valle-Levinson et al., 2004) in the Chile coastal upwelling region, the Sermilik Fjord in Greenland (Straneo et al., 2010), the Lyse Fjord in Norway (Erga et al., 2012), or the Salish Sea in the Pacific coast of North America (Giddings & Maccready, 2017). Future studies should be addressed

to determine the spatial extension and temporal persistence of this phenomenon in the Galician Rías, and in similar systems worldwide, and to assess the biogeochemical relevance of this process.

Acknowledgments
We are grateful to all the technicians, researchers and crew on board the R/V Mytilus involved in the data collection. We appreciate very valuable comments by D. Barton, X. A. Álvarez-Salgado, E. Aguiar-Fernández, C. Buckingham, L. Brannigan and T. Rippeth. B. Fernández-Castro acknowledges the fundig of a FPU travel grant (EST14/00366) from the Spanish Ministry of Education and a Juan de la Cierva-Formación fellowship (FJCI-2015–25712) from the Spanish Ministry of Economy and Competitiveness. M. Villamaña acknowledges the funding of a FPU fellowship (FPU014/05385) from the Spanish Ministry of Education. The manuscript benefited from the comments of four anonymous reviewers. Funding for this study was provided by the Spanish Ministry of Economy and Competitiveness under the research projects CTM2012–30680, and CTM2016–75451-C2-1-R to B. Mouriño-Carballido and CTM2012–35155 to M. Gilcoto. The ADCP and turbulence microstructure data can be downloaded from https://iimcloud.iim.csic.es/pydio/s/ezNjbZy7KvgcjXb.

References

Alvarez, I., DeCastro, M., Gomez-Gesteira, M., & Prego, R. (2006). Hydrographic behavior of the Galician Rias Baixas (NW Spain) under the spring intrusion of the Miño River. *Journal of Marine Systems*, *60*(1–2), 144–152. https://doi.org/10.1016/j.jmarsys.2005.12.005

Álvarez-Salgado, X. A., Roson, G., Pérez, F. F., & Pazos, Y. (1993). Hydrographic Variability Off the Rias Baixas (NW Spain) during the Upwelling Season. *Journal of Geophysical Research-*, *98*(C8), 14447–14455. https://doi.org/10.1029/93JC00458

Avicola, G. S., Moum, J. N., Perlin, A., & Levine, M. D. (2007). Enhanced turbulence due to the superposition of internal gravity waves and a coastal upwelling jet. *Journal of Geophysical Research*, *112*,C06024. https://doi.org/10.1029/2006JC003831

Barton, E., Largier, J., Torres, R., Sheridan, M., Trasviña, A., Souza, A., et al. (2015). Coastal upwelling and downwelling forcing of circulation in a semi-enclosed bay: Ria de Vigo. *Progress in Oceanography*, *134*, 1–17. https://doi.org/10.1016/j.pocean.2015.01.014

Barton, E., Torres, R., Figueiras, F. G., Gilcoto, M., & Largier, J. L. (2016). Surface water subduction during a downwelling event in a semienclosed bay. *Journal of Geophysical Research: Oceans*, *121*, 3372–3380. https://doi.org/10.1002/2015JC011421

Blanton, J. O., Tenore, K. R., Castillejo, F., Atkinson, L. P., Schwing, F. B., & Lavin, A. (1987). Relationship of upwelling to mussel production in the Rias on the western coast of Spain. *Journal of Marine Research*, *45*(2), 497–511. https://doi.org/10.1357/002224087788401115

Bouffard, D., & Boegman, L. (2013). A diapycnal diffusivity model for stratified environmental flows. *Dynamics of Atmospheres and Oceans*, *61–62*, 14–34. https://doi.org/10.1016/j.dynatmoce.2013.02.002

Burchard, H., & Hetland, R. D. (2010). Quantifying the Contributions of Tidal Straining and Gravitational Circulation to Residual Circulation in Periodically Stratified Tidal Estuaries. *Journal of Physical Oceanography*, *40*(6), 1243–1262. https://doi.org/10.1175/2010JPO4270.1

Chen, S.-N., & Sanford, L. P. (2009). Axial Wind Effects on Stratification and Longitudinal Salt Transport in an Idealized, Partially Mixed Estuary*. *Journal of Physical Oceanography*, *39*(8), 1905–1920. https://doi.org/10.1175/2009JPO4016.1

Erga, S. R., Ssebiyonga, N., Frette, Ø., Hamre, B., Aure, J., Strand, Ø., & Strohmeier, T. (2012). Dynamics of phytoplankton distribution and photosynthetic capacity in a western Norwegian fjord during coastal upwelling: Effects on optical properties. *Estuarine, Coastal and Shelf Science*, *97*, 91–103. https://doi.org/10.1016/j.ecss.2011.11.034

Figueiras, F., Labarta, U., & Fernández Reiriz, M. (2002). Coastal upwelling, primary production and mussel growth in the Rías Baixas of Galicia. *Hydrobiologia*, *484*(1/3), 121–131. https://doi.org/10. 1023/A:1021309222459

Fraga, F. (1981). Upwelling off the Galician coast, northwest Spain, *Coastal and Estuarine Sciences*, *1*, 176–182. https://doi.org/10.1029/CO001p0176

Fraga, F., & Margalef, R. (1979). Las rias gallegas. in *Estudio y explotacion del mar en Galicia* (pp. 101–121). Spain: Santiago de Compostela. Universidade de Santiago de Compostela, Santiago de Compostela.

Fréon, P., Barange, M., & Arístegui, J. (2009). Eastern Boundary Upwelling Ecosystems: Integrative and comparative approaches. *Progress in Oceanography*, *83*(1–4), 1–14. https://doi.org/10.1016/j.pocean.2009.08.001

Gargett, A. E., Osborn, T. R., & Nasmyth, P. W. (1984). Local isotropy and the decay of turbulence in a stratified fluid. *Journal of Fluid Mechanics*, *144*(1), 231. https://doi.org/10.1017/S0022112084001592

Geyer, W. R., & Farmer, D. M. (1989). Tide-induced variation of the dynamics of a salt wedge estuary. *Journal of Physical Oceanography*, *19*, 1060–1072.

Geyer, W. R., & Smith, J. D. (1987). Shear Instability in a Highly Stratified Estuary. *Journal of Physical Chemistry B*, *17*, 1668–1679.

Giddings, S. N., Fong, D. A., & Monismith, S. G. (2011). Role of straining and advection in the intratidal evolution of stratification, vertical mixing, and longitudinal dispersion of a shallow, macrotidal, salt wedge estuary. *Journal of Geophysical Research 116,*. C03003. https://doi.org/10.1029/2010JC006482

Giddings, S. N., & Maccready, P. (2017). Reverse Estuarine Circulation Due to Local and Remote Wind Forcing, Enhanced by the Presence of Along-Coast Estuaries. *Journal of Geophysical Research: Oceans*, *122*, 1–22. https://doi.org/10.1002/2016JC012479

Gilcoto, M., Álvarez-Salgado, X. A., & Perez, F. F. (2001). Computing optimum estuarine residual fluxes with a multiparameter inverse method (OERFIM): application to the Ria de Vigo (NW Spain). *Journal of Geophysical Research*, *106*(12), 31303–31318. https://doi.org/10.1029/2000JC000665

Gilcoto, M., Largier, J. L., Barton, E. D., Piedracoba, S., Torres, R., Graña, R., et al. (2017). Rapid response to coastal upwelling in a semienclosed bay. *Geophysical Research Letters*, *44*, 2388–2397. https://doi.org/10.1002/2016GL072416

Gilcoto, M., Pardo, P. C., Álvarez-Salgado, X. A., & Pérez, F. F. (2007). Exchange fluxes between the Ría de Vigo and the shelf: A bidirectional flow forced by remote wind. *Journal of Geophysical Research: Oceans*, *112*(6), 1–21. https://doi.org/10.1029/2005JC003140

Godin, G. (1972). *The analysis of tides*. (296. pp.), Buffalo: Univ. Toronto Press.

Hales, B., Moum, J. N., Covert, P., & Perlin, A. (2005). Irreversible nitrate fluxes due to turbulent mixing in a coastal upwelling system. *Journal of Geophysical Research:*, *110*,, C10S11. https://doi.org/10.1029/2004JC002685

Hansen, D. V., & Rattray, M. J. (1966). New Dimensions in estuary classification. *Limnology and Oceanography*, *11*, 319–326.

Haynes, R., & Barton, E. D. (1990). A poleward flow along the Atlantic coast of the Iberian peninsula. *Journal of Geophysical Research*, *95*(C7), 11425–11441. https://doi.org/10.1029/JC095iC07p11425

Howarth, M. J. (1998). The effect of stratification on tidal current profiles. *Continental Shelf Research*, *18*(11), 1235–1254. https://doi.org/10.1016/S0278-4343(98)00042-9

Ivey, G., Winters, K., & Koseff, J. (2008). Density Stratification, Turbulence, but How Much Mixing? *Annual Review of Fluid Mechanics*, *40*(1), 169–184. https://doi.org/10.1146/annurev.fluid.39 050905.110314

Ivey, G. N., & Imberger, J. (1991). On the Nature of Turbulence in a Stratified Fluid. Part I: The Energetics of Mixing. *Journal of Physical Oceanography*, *21*(5), 650–658. https://doi.org/10.1175/1520-0485(1991)021\ensuremath{{}0650:OTNOTI\ensuremath{}}2.0.CO;2

Jay, D. A., & Musiak, J. D. (1996). Internal tidal asymmetry in channel flows: origins and consequences. *Mixing in Estuaries and Coastal Seas*, *50*, 211–249. https://doi.org/10.1029/CE050p0211

Jeans, D., & Sherwin, T. (2001). The variability of strongly non-linear solitary internal waves observed during an upwelling season on the Portuguese shelf. *Continental Shelf Research*, *21*(16), 1855–1878. https://doi.org/10.1016/S0278-4343(01)00026-7

Kay, D. J., & Jay, D. A. (2003a). Interfacial mixing in a highly stratified estuary 2. A "method of constrained differences" approach for the determination of the momentum and mass balances and the energy of mixing. *Journal of Geophysical Research*, *108*(C3), 3073. https://doi.org/10.1029/2000JC000252

Kay, D. J., & Jay, D. A. (2003b). Interfacial mixing in a highly stratified estuary 1. Characteristics of mixing. *Journal of Geophysical Research*, *108*(C3), 3072. https://doi.org/10.1029/2000JC000252
Kurapov, A. L., Allen, J. S., & Egbert, G. D. (2010). Combined Effects of Wind-Driven Upwelling and Internal Tide on the Continental Shelf. *Journal of Physical Oceanography*, *40*(4), 737–756. https://doi.org/10.1175/2009JPO4183.1
Maas, L. R. M., & van Haren, J. J. M. (1987). Observations on the vertical structure of tidal and inertial currents in the central North Sea. *Journal of Marine Research*, *45*(2), 293–318. https://doi.org/10.1357/002224087788401106
Macdonald, D. G., & Horner-Devine, A. R. (2008). Temporal and spatial variability of vertical salt flux in a highly stratified estuary. *Journal of Geophysical Research*, *113*,. C09022. https://doi.org/10.1029/2007JC004620
McCardell, G., O'donnell, J., Souza, A. J., & Palmer, M. R. (2016). Internal tides and tidal cycles of vertical mixing in western Long Island Sound. *Journal of Geophysical Research: Oceans*, *121*, 1063–1084. https://doi.org/10.1002/2015JC010796
Michallet, H., & Barthelemy, E. (1998). Experimental study of interfacial solitary waves. *Journal of Fluid Mechanics*, *366*, 159–177. https://doi.org/10.1017/S002211209800127X
Miles, J. W. (1961). On the stability of heterogeneous shear flows. *Journal of Fluid Mechanics*, *10*, 496–508. https://doi.org/10.1143/JJAP.8.821
Monismith, S. G. (2010). Mixing in estuaries. In A. Valle-Levinson (Ed.), *Contemporary issues in estuarine physics* (pp. 145–185). Camdridge, UK: Cambridge University Press. https://doi.org/10.1017/CBO9780511676567.008
Mouriño, C., & Fraga, F. (1982). Hidrografía de la ría de Vigo. 1976–1977. Influencia anormal del río Miño, *Investigación Pesquera*, *46*(459–468).
Munk, W., & Wunsch, C. (1998). Abyssal recipes II: Energetics of tidal and wind mixing. *Deep Sea Research I*, *45*(12), 1977–2010. https://doi.org/10.1016/S0967-0637(98)00070-3
Nogueira, E., Pérez, F., & Ríos, A. (1997). Seasonal Patterns and Long-term Trends in an Estuarine Upwelling Ecosystem (Ría de Vigo, NW Spain). *Estuarine, Coastal and Shelf Science*, *44*(3), 285–300. https://doi.org/10.1006/ecss.1996.0119
Osborn, T. R. (1980). Estimates of the Local Rate of Vertical Diffusion from Dissipation Measurements. *Journal of Physical Oceanography*, *10*, 83–89. https://doi.org/10.1175/1520-0485(1980)010\ensuremath{}0083:EOTLRO\ensuremath{}2.0.CO;2
Palmer, M. R. (2010). The modification of current ellipses by stratification in the Liverpool Bay ROFI. *Ocean Dynamics*, *60*(2), 219–226. https://doi.org/10.1007/s10236-009-0246-x
Partch, E. N., & Smith, J. D. (1978). Time Dependent Mixing in a Salt Wedge Estuary. *Estuarine and Coastal Marine Science*, *6*, 3–19.
Peters, H. (1997). Observations of stratified turbulent mixing in an estuary: Neap-to-spring variations during high river flow. *Estuarine, Coastal and Shelf Science*, *45*, 69–88. https://doi.org/10.1006/ecss.1996.0180
Peters, H., & Bokhorst, R. (2000). Microstructure Observations of Turbulent Mixing in a Partially Mixed Estuary. Part I: Dissipation Rate. *Journal of Physical Oceanography*, *30*, 1232–1244. https://doi.org/10.1175/1520-0485(2001)031\ensuremath{}1105:MOOTMI\ensuremath{}2.0.CO;2
Piedracoba, S. (2005). Short-timescale thermohaline variability and residual circulation in the central segment of the coastal upwelling system of the Ría de Vigo (northwest Spain) during four contrasting periods. *Journal of Geophysical Research*, *110* C03,018. https://doi.org/10.1029/2004JC002556
Piñeiro Rodríguez, O. S. (2014). *Influencia de la marea y el viento local y remoto en la circulación en la boca sur de la ría de Vigo (Noroeste de la Península Ibérica)* (Msc thesis). Vigo, Spain: Universidade de Vigo.
Prandke, H., Holtsh, K., & Stips, A. (2000). MITEC technology development: the microstructure-turbulence measuring system (MSS. EUR 19733 EN). Italy: Ispra Joint Research Center, European Commission.
Prandke, H., & Stips, A. (1998). Test measurements with an operational microstructure-turbulence profiler: Detection limit of dissipation rates. *Aquatic Sciences*, *60*(3), 191–209. https://doi.org/10.1007/s000270050036
Prandle, D. (1982). The vertical structure of tidal currents and other oscillatory flows. *Continental Shelf Research*, *1*(2), 191–207. https://doi.org/10.1016/0278-4343(82)90004-8
Prego, R., & Fraga, R. (1990). Water interchange between the Ria of Vigo and the coastal shelf. *Scientia Marina*, *54*(1), 95–100.
Rainville, L., & Pinkel, R. (2001). Wirewalker: An autonomous wave-powered vertical profiler. *Journal of Atmospheric and Oceanic Technology*, *18*(6), 1048–1051. https://doi.org/10.1175/1520-0426(2001) 018\ensuremath{}1048:WAAWPV\ensuremath{}2.0.CO;2
Ralston, D. K., Geyer, W. R., Lerczak, J. A., & Scully, M. (2010). Turbulent mixing in a strongly forced salt wedge estuary. *Journal of Geophysical Research 115*, C12024.. https://doi.org/10.1029/2009JC006061
Ríos, A. F., Pérez, F. F., & Fraga, F. (1992). Water masses in the upper and middle North Atlantic Ocean east of the Azores. *Deep-Sea Research*, *394*(3), 645–558.
Rippeth, T. P., Palmer, M. R., Simpson, J. H., Fisher, N. R., & Sharples, J. (2005). Thermocline mixing in summer stratified continental shelf seas. *Geophysical Research Letters*, *32*,, L05602 https://doi.org/10.1029/2004GL022104
Rippeth, T. P., Wiles, P. J., Palmer, M. R., Sharples, J., & Tweddle, J. (2009). The diapcynal nutrient flux and shear-induced diapcynal mixing in the seasonally stratified western Irish Sea. *Continental Shelf Research*, *29*(13), 1580–1587. https://doi.org/10.1016/j.csr.2009.04.009
Rippeth, T. T., Fisher, N. N., & Simpson, J. J. (2001). The cycle of turbulent dissipation in the presence of tidal straining. *Journal of Physical Oceanography*, *31*(8), 2458–2471. https://doi.org/10.1175/1520-0485(2001)031\ensuremath{}2458:TCOTDI\ensuremath{}2.0.CO;2
Scully, M. E., Friedrichs, C., & Brubaker, J. (2005). Control of Estuarine Stratification and Mixing by Wind-Induced Straining of the Estuarine Density Field. *Estuaries*, *28*(3), 321–326. https://doi.org/10. 2307/3526916
Scully, M. E., & Friedrichs, C. T. (2007). Sediment pumping by tidal asymmetry in a partially mixed estuary. *Journal of Geophysical Research*, *112*,.C07028. https://doi.org/10.1029/2006JC003784
Scully, M. E., & Geyer, W. R. (2012). The Role of Advection, Straining, and Mixing on the Tidal Variability of Estuarine Stratification. *Journal of Physical Oceanography*, *42*(5), 855–868. https://doi.org/10.1175/JPO-D-10-05010.1
Shih, L. H., Koseff, J. R., Ivey, G. N., & Ferziger, J. H. (2005). Parameterization of turbulent fluxes and scales using homogeneous sheared stably stratified turbulence simulations. *Journal of Fluid Mechanics*, *525*, 193–214. https://doi.org/10.1017/S0022112004002587
Simpson, J. H., Brown, J., Matthews, J., & Allen, G. (1990). Tidal Straining, Density Currents, and Stirring in the Control of Estuarine Stratification. *Estuaries*, *13*(2), 125. https://doi.org/10.2307/1351581
Simpson, J. H., Williams, E., Brasseur, L. H., & Brubaker, J. M. (2005). The impact of tidal straining on the cycle of turbulence in a partially stratified estuary. *Continental Shelf Research*, *25*(1), 51–64. https://doi.org/10.1016/j.csr.2004.08.003
Soulsby, R. L. (1983). Chapter 5 The Bottom Boundary Layer of Shelf Seas, *Physical Oceanography of Coastal and Shelf Seas*, *35*, 189–266, https://doi.org/10.1016/S0422-9894(08)70503-8
Sousa, M. C., Mendes, R., Alvarez, I., Vaz, N., Gomez-Gesteira, M., & Dias, J. M. (2014). Unusual circulation patterns of the rias baixas induced by minho freshwater intrusion (NW of the Iberian Peninsula). *PLoS ONE*, *9*(11), https://doi.org/10.1371/journal.pone.0112587
Souto, C., Gilcoto, M., Fariña-Busto, L., & Pérez, F. F. (2003). Modeling the residual circulation of a coastal embayment affected by wind-driven upwelling: Circulation of the Ría de Vigo (NW Spain). *Journal of Geophysical Research*, *108*(C11), 3340. https://doi.org/10.1029/2002JC001512

Souza, A. J., & Simpson, J. H. (1996). The modification of tidal ellipses by stratification in the Rhine ROFI. *Continental Shelf Research*, *16*(8), 997–1007. https://doi.org/10.1016/0278-4343(95)00042-9

Stacey, M. T., Monismith, S. G., & Burau, J. R. (1999). Observations of Turbulence in a Partially Stratified Estuary. *Journal of Physical Oceanography*, *29*(8), 1950–1970. https://doi.org/10.1175/1520-0485(1999)029\ensuremath{⟨}1950:OOTIAP\ensuremath{⟩}2.0.CO;2

Stacey, M. T., & Ralston, D. K. (2005). The Scaling and Structure of the Estuarine Bottom Boundary Layer. *Journal of Physical Oceanography*, *35*(1), 55–71. https://doi.org/10.1175/JPO-2672.1

Straneo, F., Hamilton, G. S., Sutherland, D. A., Stearns, L. A., Davidson, F., Hammill, M. O., et al.. (2010). Rapid circulation of warm subtropical waters in a major glacial fjord in East Greenland. *Nature Geoscience*, *3*(3), 182–186. https://doi.org/10.1038/ngeo764

Thorpe, S. (2007). *An Introduction to ocean turbulence* (240. pp.). New York: Cambridge University Press, https://doi.org/10.1029/2008EO520011

Thorpe, S. A. (1977). Turbulence and Mixing in a Scottish Loch. *Philosphical Transactions of Royal Society of London A*, *286*(1334), 125–181. https://doi.org/10.1098/rsta.1977.0112

Valle-Levinson, A. (2003). Flow induced by upwelling winds in an equatorward facing bay: Gulf of Arauco, Chile. *Journal of Geophysical Research*, *108*(C2),3054. https://doi.org/10.1029/2001JC001272

Valle-Levinson, A., Schneider, W., Sobarzo, M., Bello, M., Bravo, L., Castillo, M., et al. (2004). Wind-induced exchange at the entrance to Concepción Bay, an equatorward facing embayment in central Chile. *Deep-Sea Research Part II*, *51*(20–21), 2371–2388. https://doi.org/10.1016/j.dsr2.2004.08. 010

Varela, R. A., Rosón, G., Herrera, J. L., Torres-López, S., & Fernández-Romero, A. (2005). A general view of the hydrographic and dynamical patterns of the Rías Baixas adjacent sea area. *Journal of Marine Systems*, *54*, 97–113. in p https://doi.org/10.1016/j.jmarsys.2004.07.006

Villacieros-Robineau, N., Herrera, J. L., Castro, C. G., Piedracoba, S., & Roson, G. (2013). Hydrodynamic characterization of the bottom boundary layer in a coastal upwelling system (Ría de Vigo, NW Spain). *Continental Shelf Research*, *68*, 67–79. https://doi.org/10.1016/j.csr.2013.08.017

Villamaña, M., B., Mouriño-Carballido, E., Marañón, P., Cermeño, P., Choucino, J. C. B., da Silva, P. A., et al. (2017). Role of internal waves on mixing, nutrient supply and phytoplankton community structure during spring and neap tides in the Ría de Vigo (NW Iberian Peninsula). *Limnology and Oceanography: Methods*, *62*(3), 1014–1030. https://doi.org/10.1002/lno.10482

Whitney, M. M., Codiga, D. L., Ullman, D. S., McManus, P. M., & Jiorle, R. (2012). Tidal Cycles in Stratification and Shear and Their Relationship to Gradient Richardson Number and Eddy Viscosity Variations in Estuaries. *Journal of Physical Oceanography*, *42*(7), 1124–1133. https://doi.org/10.1175/JPO-D-11-0172.1

Wooster, W. S., Bakun, A., & McLain, D. R. (1976). Seasonal upwelling cycle along the eastern boundary current of the North Atlantic. *Journal of Marine Research*, *34*(2).

Xie, X., & Li, M. (2018). Effects of wind straining on estuarine circulation: A combined observational and modeling study. *Journal of Geophysical Research: Oceans*, *123*. https://doi.org/10.1002/2017JC013470